Draft version September 11, 2026
Typeset using LaTeX **twocolumn** style in AASTeX631

A Catalog of Beta Cep Stars and Their Characterization

Noi Shitrit[1] Gerald Handler[2] Iair Arcavi[1] F. Kahraman Aliçavuş[3,4] Mathijs Vanrespaille[5]
Conny Aerts[5] Sowgata Chowdhury[2] Andrzej Pigulski[6] Michał Nowak,[7] John Hoffman,[8]
Jonathan Labadie-Bartz[9] Grzegorz Pojmański[7] Gaspar Á. Bakos[8] Igor Soszyński[10]
Dominic Bowman[11] Keegan Thomson-Paressant[11] Keivan G. Stassun[12] and - order is TBD

[1]*The School of Physics and Astronomy, Tel Aviv University, Tel Aviv 69978, Israel*
[2]*Nicolaus Copernicus Astronomical Center (NCAC), Polish Academy of Sciences, 00-716 Warsaw, Poland*
[3]*Çanakkale Onsekiz Mart University, Science Faculty, Physics Department, 17100, Canakkale, Türkiye*
[4]*Çanakkale Onsekiz Mart University, Astrophysics Research Center and Ulupınar Observatory, TR-17100, Çanakkale, Türkiye*
[5]*Institute of Astronomy, KU Leuven, Celestijnenlaan 200D, B-3001 Leuven, Belgium*
[6]*Astronomical Institute Wrocław University, ul. Kopernika 11, 51-622 Wrocław, Poland*
[7]*Warsaw University Observatory, 00-478 Warsaw, Poland*
[8]*Department of Astrophysical Sciences, Princeton University, NJ 08544, USA*
[9]*Lehigh University, Physics Department, Bethlehem, PA, 18015, USA*
[10]*Astronomical Observatory, University of Warsaw, Al. Ujazdowskie 4, 00-478 Warszawa, Poland*
[11]*School of Mathematics, Statistics and Physics, Newcastle University, Herschel Building, Newcastle upon Tyne, NE1 7RU, United Kingdom*
[12]*Vanderbilt University, Department of Physics & Astronomy, 6301 Stevenson Center Lane, Nashville, TN 37235, USA*

ABSTRACT

β Cep stars are pulsating late O- and early B-type stars. Their oscillations provide valuable constraints on the internal structure of massive stars through asteroseismology. In the past two decades, space telescopes and comprehensive ground-based sky surveys have enabled the detection of hundreds of new β Cep candidate pulsators. In this work, we collect all reported β Cep stars in the literature since the last catalog was published more than two decades ago, and perform an archival search of several ground-based surveys, resulting in a total sample of 2,543 β Cep candidate stars (of which 499 are newly reported here). We collect spectra for 67 selected stars, which we analyze and model to derive stellar parameters and compare with Gaia estimates. We perform visual classification of each of the 2,421 stars with available TESS data by inspecting their light curves, periodograms, spectral types and temperatures, to re-classify all stars. We confirm 1,130 β Cep pulsators in total, including hybrids and eclipsing binary systems, of which 180 are newly reported here, and an additional 246 β Cep candidate stars, of which 18 are newly reported here. This constitutes an order of magnitude increase in the number of stars since the previous catalog. We reject 1,045 stars as β Cep pulsators and reclassify most of them as candidate slowly pulsating B-type, δ Scuti, or γ Doradus pulsators. We apply frequency analysis to all stars classified as β Cep stars and perform statistical analyses of their stellar and pulsation parameters. This catalog presents the largest compilation of β Cep pulsators to date, including pulsation parameters and reliable visually classified pulsators for use in future studies.

Keywords: Ground-based astronomy (686) — Astronomical methods (1043) — Astronomical techniques (1684) — Observational astronomy (1145) — Massive stars (732) — Asteroseismology (73) — Stellar interiors (1606)

Corresponding author: Noi Shitrit
noish26@gmail.com

1. INTRODUCTION

Massive stars play a fundamental role in astrophysics. These stars experience strong stellar winds, emit ionizing radiation, and most end their lives in core-collapse supernovae, leaving behind compact remnants. Understanding these phenomena, which is essential for building a complete picture of both stellar and galactic evolution, requires a detailed understanding of the internal structure and physical processes of massive stars.

Asteroseismology provides a way to probe the internal structure and evolution of massive stars by studying their pulsations, which can reveal internal rotation profiles, convective core sizes and the extent of mixing in radiative zones. β Cep stars are late O- and early B-type, spanning a mass range of ∼8-25 $M_\odot$. Their oscillations are primarily driven by the opacity (κ-) mechanism of iron-peak elements (Moskalik & Dziembowski 1992; Dziembowski & Pamiatnykh 1993), which causes periodic variations in opacity. They oscillate in low-order pressure (p) modes with periods between approximately 2 and 8 hours (Stankov & Handler 2005; Aerts et al. 2010; Bowman 2020). Some β Cep stars also oscillate in high-order gravity (g) modes with longer periods of more than a day (Handler et al. 2006a, 2009).

HD 129929 was the first β Cep star for which a complete asteroseismic analysis, including mode identification (i.e., identifying the harmonic degree l and azimuthal order m of each mode; Aerts et al. 2003), was performed. They observed the star for more than 21 years from the ground and constrained the core-overshooting parameter, metallicity, the rotation rate of the star, and were the first to rule out rigid rotation. A more recent example is provided by Burssens et al. (2023), who used a long-baseline, semi-continuous TESS light curve of the β Cep star HD 192575 to constrain the mass of the convective core and identify non-rigid rotation in its interior.

The last compilation of β *Cep* stars was published over two decades ago by Stankov & Handler (2005) who reviewed more than 250 papers covering ∼100 years of literature and gathered 231 candidates. Of these, 93 were confirmed as β Cep stars, 77 were classified as candidate β Cep stars due to limited or insufficient data, while the remaining 61 were rejected as β Cep candidates. Among the confirmed β Cep stars, the pulsation periods ranged between 1.6 to 7.66 hours (corresponding to $3.1348 - 14.9925$ cycles/day) and the spectral types spanned B0-B2. However, since spectral classifications are not always accurate, Stankov & Handler (2005) broadened the spectral range defining β Cep stars to span from O7 to B3.

Ground-based surveys such as the Optical Gravitational Lensing Experiment (OGLE; Udalski et al. 1992), the All Sky Automated Survey (ASAS; Pojmanski 1997a; Pojmański 2001a), the Hungarian Automated Telescope (HAT; Bakos et al. 2004a), the Kilodegree Extremely Little Telescope (KELT; Pepper et al. 2007, 2012), the All-Sky Automated Survey for Supernovae (ASAS-SN; Kochanek et al. 2017), and the Zwicky Transient Facility (ZTF; Bellm et al. 2019) collected and published new data. Additionally, space-based missions like the Convection, Rotation and planetary Transits (CoRoT) mission, Kepler (Borucki et al. 2010), the Transiting Exoplanet Survey Satellite (TESS; Ricker et al. 2015) and Gaia (Gaia Collaboration et al. 2016) were launched. These surveys and missions have produced large amounts of new photometry, and as a result, new identifications of β Cep candidates have been published. In addition, space-based missions, with their long time baselines for many stars, allow for more accurate frequency analyses, which can help reclassify β Cep candidates and perform more accurate asteroseismological studies of them.

These new data have also deepened our physical understanding of β Cep pulsations. Pulsation periods longer than about 6 hours in some β Cep stars can result from high-order gravity modes that are excited to observable amplitudes by rapid rotation (Ushomirsky & Bildsten 1998; Townsend 2000), as seen, for example, in the β Cep stars HD 203664 (Aerts et al. 2006) and V986 Oph (Handler et al. 2012a).

Up to this date, there are only several β Cep stars with a complete asteroseismic modeling, including mode identification for all the dominant pulsation modes of the star (Aerts et al. 2003; Aerts 2000; De Ridder et al. 2004; Handler et al. 2005, 2006b, 2012b). These type of studies usually require multi-band ground-based data complementary to the space data, to enable mode identification to the dominant modes, without relying on rotational splitting, that is not always possible.

The Global Asteroseismology Project (GAP) aims to triple the number of studied massive stars with a complete asteroseismic analysis, combining space- and ground-based continuous photometry (Shitrit & Arcavi 2024). The project was awarded 9000 observing hours over three years on the 0.4 m telescopes of the Las Cumbres Observatory network Brown et al. (2013). GAP is collecting multi-band, high-cadence data of ∼ 20 β Cep stars to complement the single-band TESS data. This will allow complete seismological studies, including mode identification , of a sample of massive stars, almost tripling the current sample with a complete asteroseismic study.

Fritzewski et al. (2025a) used the multi-band data from Gaia together with a probabilistic framework based on the known dominant modes of six previously studied β Cep stars to perform mode identification for 119 TESS-observed β Cep stars, using theoretical and observed amplitude ratios to determine the dominant mode in each case. This work represents a significant step toward large-scale asteroseismology of β Cep stars using modern TESS and Gaia data combined with earlier ground-based studies. Vanrespaille et al. (2026) extend this work by performing forward modeling and asteroseismic analysis for a subsample of the Fritzewski et al. (2025a) stars, selecting those for which partial mode identification could be obtained from rotational splitting.

Eze & Handler (2024) identified 59 new β Cep stars in eclipsing binary (EB) systems using TESS data. This sample provides a foundation for follow-up observations and modeling of β Cep stars in binaries and enables meaningful comparisons with their single-star counterparts.

New and upcoming surveys and modeling techniques such as these motivate the need for an updated β Cep catalog. Here, we do just that by incorporating new observations and analyses of known β Cep stars, together with candidates newly identified in this work and in the literature published since the compilation by Stankov & Handler (2005). Our comprehensive catalog and analysis we present here incorporate literature published until January 2026. We are aware that several papers published since identify additional β Cep candidates that may not be included in this work (e.g., Thomson-Paressant et al. 2026.)

In Section 2, we explain how our catalog was constructed. In Section 3, we describe the sources of the photometric data used, together with the light-curve and frequency analysis. In Section 4, we present our spectroscopic observations, along with the spectral analysis and modeling. In Section 5, we outline the visual inspection and classification process. In Section 6, we present the classification results. In Section 7, we present a statistical analysis of the stars in the catalog. We summarize our work in Section 8.

2. COMPILING THE CATALOG

We compile objects for our catalog through two channels: a literature review of reported β Cep stars, and our own search for new β Cep stars through light-curve analysis of archival data.

2.1. *Literature Review*

We review the literature published since the Stankov & Handler (2005) catalog (including a few β Cep publications from before the Stankov & Handler 2005 catalog) until January 2026, focusing on papers that discuss, in their titles and abstracts, β Cep stars, asteroseismology of massive stars and classification of pulsators. We find 217 papers (including Stankov & Handler 2005), among which 72 papers report newly identified β Cep stars (Table A1 in Appendix A). Additionally, we include all the β Cep classification designations from the SIMBAD Astronomical Database (Wenger et al. 2000) that do not include a reference to their classification, as well as stars classified as β Cep stars in the International Variable Star Index (VSX; Watson et al. 2022). In total, from the literature search, after removing duplicates, the literature search yields 2,044 candidate β Cep stars. We present the full list of references and the number of objects in each reference in Table A1. We retrieve data for the stars in the catalog, including their spectral type, V-band magnitude, and pulsation classification from SIMBAD (Wenger et al. 2000) when available.

2.2. *Archival Data Search*

In addition to our literature survey, we inspect light curves from ASAS (Pojmanski 1997b; Pojmański 2001b), the HAT system (Bakos et al. 2004b) and the fourth phase of OGLE (OGLE-IV; Udalski et al. 2015) sky surveys for new possible β Cep stars.

We conduct the search for candidates together with Labadie-Bartz et al. (2020), who performed the archival search of the KELT data. We follow the same protocol as Labadie-Bartz et al. (2020) to select the candidates and briefly summarize it here. We cross-match all stars with spectral classifications between O4–B7 with the survey light curves and examine the matched stars for the presence of pulsations that fall within the β Cep frequency range by performing frequency analysis of the light curves.

We check the literature for possible misclassifications, for example cases with uncertain spectral types or published spectroscopic effective temperatures inconsistent with β Cep stars. In addition, we use Gaia parallaxes (Gaia Collaboration et al. 2016, 2023a) to estimate stellar luminosities and reject objects whose luminosities are too low for β Cep stars such as δ Scuti stars or gravity-mode sub-dwarf B (sdB) pulsators.

This search, from ASAS, HAT surveys and OGLE-IV, yields a total of 949 β Cep candidates, of which 499 are newly reported candidate β Cep stars. Of these, 4 do not have a TESS light curve and we do not classify them in this work. In total, together with the literature and the photometric search, the complete list of β Cep candidates with which we begin the reclassification process contains 2,543 candidates (see Table 1 for a summary of the number of objects).

3. PHOTOMETRIC DATA

3.1. *Cross-Matching with TESS and Gaia*

Table 1. Summary of the number of candidates identified in the literature and archival searches.

Literature review - no duplicates	2,044
Archival review - total	949
Archival review - newly reported	499
Complete candidate list - this work, no duplicates	2,543

We first cross-match all coordinates of the candidates, taken from the SIMBAD catalog when available, and otherwise from their original references (or the relevant photometric survey in the case of archival-search candidates), with the Gaia Data Release 3 (DR3) catalog, using an initial search radius of $1''$. For objects without a Gaia match within $1''$, we repeat the search using a radius of $2''$ and inspect the possible matches individually. When more than one source is found within the applied search radius, we select the source with the brightest Gaia G-band magnitude. We identify these 23 objects using the *Gaia_MULT_MATCH* column, where a value of 1 indicates multiple physical Gaia candidates and 0 indicates a single or no candidate.

In total, we find a Gaia DR3 source ID for 2,526 out of our 2,543 candidates. For the remaining 17 stars not found in the Gaia archive, we retain their SIMBAD coordinates. For stars with no Gaia match, we retain the original coordinates, otherwise, we use the Gaia coordinates. Of the 2,526 Gaia sources, 1,695 have outputs from the Generalized Stellar Parametrizer Photometry (GSP-Phot) pipeline (Creevey et al. 2023). This pipeline estimates global stellar parameters such as effective temperature, surface gravity and metallicity using the basic Gaia observables, including the flux ratio between the blue and red photometric bands and parallaxes.

In addition, 1,882 stars have outputs from the Extended Stellar Parametrizer for Hot Stars (ESP-HS; Fouesneau et al. 2023) pipeline. Following Fritzewski et al. (2025a) and Shi et al. (2023), we adopt the ESP-HS parameters when available, as they are more reliable for hot pulsating main-sequence stars.

Next, we use the coordinates of all candidates to perform a cross-match with the TESS Input Catalog (TIC), adopting an initial search radius of $1''$. For objects already identified by a TIC designation, we retain that TIC identifier. For objects without a TIC match within $1''$, we repeat the search using a radius of $2''$ and inspect the possible matches individually. When multiple physical TIC sources are found within $1''$, we inspect the candidates individually and select the appropriate source. We identify these 13 objects using the *TIC_MULT_MATCH* column, where a value of 1 indicates multiple physical TIC candidates and 0 indicates a single or no candidate. We successfully match 2,542 of the 2,543 stars in the catalog to a TIC entry, but only 2,421 stars have a TESS light curve in the Mikulski Archive for Space Telescopes (MAST; see Section 3.2). The remaining 122 stars do not have TESS light curves and are either too bright or too faint (fainter than the QLP data faint magnitude limit), or are located in overly crowded fields. We therefore do not visually classify them in this work.

3.2. *Light Curves and Frequency Analysis*

For each star with TESS photometry, we use light curves from both the Science Processing Operations Center (SPOC; Jenkins et al. 2016) and the Quick-Look Pipeline (QLP; Huang et al. 2020)[1]. The SPOC pipeline generally provides higher-precision light curves, but not all stars have SPOC light curves, and not all sectors in which a star is observed are processed by SPOC. Therefore, we use SPOC light curves when available and analyze all available QLP light curves as well. Out of the total of 2,543 stars, 1,292 stars have SPOC data, and 2,413 have QLP data.

For each light curve, we apply the following processing steps. We first remove all NaN values from the data. Then, for each sector, we normalize the raw flux measurements and their uncertainties relative to the median flux of the star in that sector. Specifically, we subtract the sector median from each flux value and divide the result by that median, while dividing the flux uncertainties by the same median. This operation removes sector-to-sector zero-point offsets introduced by instrumental effects while preserving the relative variability amplitudes within each segment, resulting in a light curve normalized around zero, with values given in fractional (relative) flux and uncertainties expressed in relative units. Since the QLP output is in detector units, we use these units consistently for both the QLP and SPOC data.

Since not all sectors are observed with the same cadence, following Fritzewski et al. (2025a), we equalize the cadence (hereafter referred to as "binning") by binning the shorter-cadence sectors to the longest exposure time available for that star to prevent inhomogeneous data sampling, which could bias the frequency analysis. Here, we use both cadence-equalized light curves and the light curves at the original cadence, and compare the results.

[1] We download all light curves using the *Lightkurve* package (Lightkurve Collaboration et al. 2018), which extracts the data from the MAST portal

Additionally, we perform sigma-clipping of the data, per sector or globally, when needed, using the values recorded in the visual classification process for each star (see Section 5).

For the frequency analysis, we extract the pulsation frequencies, amplitudes and phases using a prewhitening process. Before applying this process, we subtract the mean time value from the complete time stamp array to reduce correlations between phases and frequencies, which improves subsequent frequency extraction.

For the prewhitening process, we use STAR SHADOW (IJspeert et al. 2024), which is an automated time-domain framework designed originally for modeling of EB variability together with intrinsic stellar oscillations in space-based photometry like that from TESS. The code constructs a global model consisting of harmonic components describing any orbital signal (if present) together with additional sinusoidal terms representing intrinsic variability. Candidate periodicities are identified using both a Lomb-Scargle algorithm and phase-dispersion minimization (PDM), after which the full multi-component model is optimized directly in the time domain using non-linear regression. We use the "star_shadow_asteroseismology" version[2] updated by M. Vanrespaille.

STAR SHADOW applies two complementary statistical criteria during the computation. The first is the Bayesian Information Criterion (BIC):

$$\mathrm{BIC} = k \ln N - 2 \ln \hat{L},$$

where k is the number of free parameters in the model, N is the total number of data points in the light curve, and $\hat{L}$ is the maximum likelihood of the fitted model. In the original STAR SHADOW, a $\Delta\mathrm{BIC} > 2$ threshold is used by default and is always enabled.

The second criterion is a false-alarm calibrated signal-to-noise (SNR) threshold following Baran & Koen (2021), where the threshold corresponds to a false-alarm probability of 0.1% and depends explicitly on the number of data points. The user can either enable this criterion together with the BIC threshold or disable it.

In the version we use, the BIC threshold can be changed. We adopt $\Delta\mathrm{BIC} > x$, where we set $x = 2$ for data with one TESS sector, $x = 6$ for two TESS sectors, and $x = 10$ for more than two TESS sectors. This increasing BIC threshold requires progressively stronger evidence before adding an additional sinusoid, thereby preventing overfitting and the detection of numerous low-amplitude frequencies in datasets with a larger number of TESS sectors. We choose to use only the BIC threshold and turn off the SNR threshold.

Since STAR SHADOW is designed to model EB variability on top of the intrinsic stellar oscillations, it also computes 19 EB system parameters for light curves with detected eclipses.

The STAR SHADOW pipeline produces a sequence of output files corresponding to successive analysis stages applied to stellar light curves, where at each stage, new parameters are computed and existing parameters are recomputed. The intrinsic stellar oscillations are computed for the first time in early stages, and the parameters of the EB system are derived at later stages. While early stages are always executed (for a valid light curve), later stages are only reached if the data satisfy specific criteria, such as the presence of significant harmonic structure or eclipse signatures. At some of the later stages, the pulsation parameters (frequencies, amplitudes, and phases) are recomputed based on the EB parameters determined at those stages.

The extraction and refinement of sinusoidal variability, represented by frequencies, amplitudes, and phases, are performed iteratively across several stages. Thus, the initial frequency extraction is recomputed based on the EB parameters derived after inferring the orbital parameters from the raw light curves. Therefore, we define an *EB_SCORE* flag that counts how many of the 19 EB system parameters are computed for each star. We consider stars with *EB_SCORE* $\geq$ 17 to be EBs (according to STAR SHADOW, regardless of the visual classification), and for these stars, we use the pulsation parameters computed at the final stage of the STAR SHADOW analysis. For stars with *EB_SCORE* $<$ 17, we adopt the pulsation parameters obtained from the initial frequency extraction stage.

Another point to note is that tidally excited oscillations in eclipsing binaries are at risk of being misclassified as orbital harmonics. Tidally excited pulsations naturally occur at integer multiples of the orbital frequency due to resonant tidal forcing, and the analysis procedure explicitly enforces this by matching frequencies within a tolerance to exact orbital harmonics. As a result, genuine pulsations located at $n \cdot f_{\mathrm{orb}}$ may be absorbed into the harmonic model and excluded from the non-harmonic frequency list, representing a known limitation (IJspeert et al. 2024).

3.3. *Bolometric Corrections and Luminosities*

To estimate the bolometric luminosity of each star, we use the temperatures from the ESP-HS pipeline, following the methodology suggested by Pedersen et al. (2020). We derive the bolometric corrections for the Gaia G, BP,

[2] https://github.com/Mathijs-Vanrespaille/star_shadow_asteroseismology/tree/mathijs_changes

and RP bands using the metallicity estimates from the GSP-Phot pipeline and the $\log g$ values (where g is the surface gravity) from the ESP-HS pipeline. For all the calculations described below, we derive one set of values using the available GSP-Phot metallicities and another assuming solar metallicity. This allows us to assess the effect of the metallicity assumption and obtain luminosity estimates for stars without GSP-Phot metallicities. We compare the resulting luminosity and extinction estimates, together with their available sample sizes, in Appendix B.

To correct the Gaia magnitudes for interstellar extinction, we obtain three-dimensional reddening estimates from the Bayestar19 dust map (Green et al. 2019) using the Gaia coordinates and inverse-parallax distances. We query the 16th, 50th, and 84th percentiles of the color excess $E(B-V)$, adopt the median as the reddening estimate, and estimate its uncertainty as half the difference between the 84th and 16th percentiles. We convert the reddening into the extinctions A_G, A_{BP}, and A_{RP} using the coefficients of Pedersen et al. (2020).

Following Pedersen et al. (2020), we combine each Gaia apparent magnitude with its corresponding bolometric correction and extinction to calculate G-, BP-, and RP-band bolometric magnitudes. We adopt their inverse-variance-weighted mean as our three-band bolometric magnitude. Because reliable Bayestar19 reddening estimates are not available for every star, we also calculate a G-band bolometric magnitude using A_G provided directly by ESP-HS. This method requires only the ESP-HS parameters and Gaia G-band photometry, thereby providing an independent extinction-based luminosity estimate for a larger sample of stars.

We convert the resulting bolometric magnitudes into $\log(L/L_\odot)$ using inverse-parallax distances. We restrict the luminosity calculations to stars with positive parallaxes and reliable Gaia astrometry, defined as RUWE < 1.4 and *parallax_over_error*¿5. We propagate the available uncertainties in the Gaia photometry, ESP-HS effective temperature and surface gravity, GSP-Phot metallicity, extinction, and parallax.

The publication catalog includes the Bayestar19 extinction, extinction-corrected absolute magnitudes, and final luminosity estimates computed and used in this work.

4. SPECTROSCOPIC OBSERVATIONS AND ANALYSIS

We collect spectra for 67 southern-hemisphere β Cep candidates using the High-Resolution Spectrograph (HRS; Bramall et al. 2010, 2012; Crause et al. 2014) mounted on the South African Large Telescope (SALT; Buckley et al. 2006). We select these stars by considering all southern-hemisphere stars in our sample and assigning each star a ranking based on the number of pulsation modes detected from the ground, its observability with TESS, and its apparent magnitude (and hence expected variability detection level). The selected 67 stars are those that rank the highest, are observable with SALT, and do not yet have high-resolution spectra available. Here, we discuss the spectroscopic observations conducted, as well as the data reduction, analysis, and modeling applied to the data.

The HRS operates in three modes: low (resolving power $R \approx 14,000$), medium ($R \approx 40,000$) and high ($R \approx 65,000$) resolution. Among the 67 stars in our sample, we observe 45 in high resolution mode, 18 in medium resolution, 3 in low resolution, while we observe one star in both medium and low resolution modes. In total, we obtain 101 spectra for the 67 stars. For 40 of them, we obtain at least two spectral epochs to perform a preliminary check for possible radial-velocity variations. We present the spectral log in Table C2 in Appendix C.

We reduce the spectra using the PySALT User Package[3] (Crawford et al. 2010). We then normalize the spectra using the *continuum* task of the National Optical Astronomy Observatories (NOAO) optical astronomy package within the Image Reduction and Analysis Facility (IRAF)[4].

We check the normalization of each spectrum by comparing it with theoretical spectra, which we calculate using the non-local thermodynamic equilibrium (NLTE) TLUSTY BSTAR2006 (Hubeny & Lanz 1995) grid assuming solar abundances. We generate these initial theoretical spectra using the spectral types listed in Table C2 in Appendix C and adopt an average projected rotational velocity ($v \sin i$, where i is the inclination) from Cox (2000). We consider the continuum placement satisfactory when the differences between the observed and theoretical continua remain within the noise level of the spectrum. In cases where noticeable deviations are present, we re-normalize the spectra until we achieve a consistent continuum level.

We further compare the normalized spectra with the same initial theoretical spectra in order to investigate the possible presence of flux contributions from secondary components. In addition, we examine radial-velocity shifts using the cross-correlation technique. The comparison between observed and theoretical line pro-

[3] http://pysalt.salt.ac.za/

[4] https://iraf.readthedocs.io/en/doc-autoupdate/tasks/noao/

files, together with the detected radial-velocity variations and line asymmetries, reveals that several stars are likely members of binary systems. We identify ALS 1135, ALS 4680, HD 81370, HD 116538, HD 171141, and HD 172367 as candidate systems. We subsequently analyze the remaining stars under the assumption of single-star spectra because they do not show clear evidence of multiplicity within the available spectra. For stars with more than one spectrum, we combine the spectra (after correcting any measured radial velocity shifts) in order to improve the signal-to-noise ratio (SNR) and to reduce possible pulsational effects on the line profiles.

To determine the value of $v \sin i$, we apply the profile-fitting method (Gray 2005) to the profiles of the He II ($\lambda = 4026$ Å) and He I ($\lambda = 4387$ Å) lines, using limb-darkened and instrumentally broadened models calculated in steps of $1\,\mathrm{km\,s^{-1}}$. We obtain the results by minimizing the differences between the observed and theoretical spectra, following the procedure described in Catanzaro et al. (2004). We estimate the uncertainties in $v \sin i$ using the $\Delta\chi^2$ criterion by considering the range of models around the minimum χ^2 solution corresponding to the 1σ confidence interval.

To determine the stellar atmospheric parameters, namely the effective temperature ($T_{\rm eff}$) and surface gravity ($\log g$), we compare the observed $H\beta$ and $H\gamma$ Balmer line profiles with the NLTE TLUSTY BSTAR2006 (Hubeny & Lanz 1995) model grid assuming solar abundances. We adopt the $v \sin i$ values derived in the previous step as an input parameter for the synthetic spectra. The model grid covers a $T_{\rm eff}$ range of $15\,000 - 30\,000$ K in steps of 1 000 K and a surface gravity range of $1.75 - 4.75$ dex in steps of 0.25 dex.

We derive the atmospheric parameters using the same profile-fitting approach that we apply for the $v \sin i$ determination, by minimizing the differences between the observed and theoretical Balmer line profiles. The best-fit model within the TLUSTY BSTAR2006 grid provides the initial estimates of $T_{\rm eff}$ and $\log g$, after which we perform linear interpolation between neighboring models to refine the $\log g$ value. We adopt an uncertainty of 1 000 K for $T_{\rm eff}$, corresponding to the temperature spacing of the model grid, while we estimate the uncertainty in $\log g$ using the $\Delta\chi^2$ criterion, considering the range of solutions around the minimum χ^2 value corresponding to the 1σ confidence interval. We list the derived atmospheric parameters and their uncertainties in Table C2 in Appendix C. Figure 1 shows three examples of the resulting theoretical fits to the observed $H\beta$ line profiles.

We find four stars to have $T_{\rm eff}$ below 15 000 K (HD 73918, HD 75290, HD 151158, and HD 151654). These $T_{\rm eff}$ values are significantly lower than expected for β Cep stars. In addition, two stars exhibit $T_{\rm eff}$ values that are highly inconsistent with their spectral classifications reported in the literature. HD 151158 is classified as B2Ib/II in the literature (Houk 1978), whereas our spectroscopic analysis yields a $T_{\rm eff}$ of only 6900 K. Similarly, HD 151654 is classified as F0V in the literature (Houk & Swift 1999), while our analysis results in a significantly higher $T_{\rm eff}$ of 13 000 K. Therefore, we conclude that the spectral classifications of these stars in the literature are incorrect.

5. VISUAL INSPECTION AND CLASSIFICATION

Identifying β Cep stars based on automated frequency-range selection from the prewhitening analysis can lead to misclassifications of impostors (see Figure D2 in Appendix D). To avoid this, we perform systematic visual inspection of all β Cep candidates using a graphical user interface (GUI) we develop. The GUI displays the TESS light curve and the Lomb–Scargle periodogram for each star, together with its prior classification, spectral type and Gaia effective temperature when available. The GUI allows us to sigma-clip each light curve, recalculate the periodogram following sigma clipping, and save user notes for each object. The GUI is available at X, and we show an example screenshot in Figure D3 in Appendix D. **a link will be added.**

5.1. *Possible Impostors*

One type of β Cep impostor we wish to exclude is that of Slowly Pulsating B-type (SPB) stars. SPB stars have a mass of approximately 3–8 $M_\odot$ and pulsation periods of ∼0.3–5 days, but some also display β Cep-type pulsations and are classified as hybrid β Cep stars. However, in some cases, the pulsations in the β Cep range are actually harmonics of the SPB pulsations, making these stars β Cep impostors (Kurtz et al. 2015). In some cases, these harmonic frequencies reach higher amplitudes than the intrinsic low-frequency modes, which increases the risk of misclassifying the star as a β Cep pulsator. An example of such an impostor we encounter in our classification process is HD 67600, which was previously classified as a β Cep star (Pigulski & Pojmański 2008a), but TESS data reveal that the pulsations within the β Cep frequency range are in fact harmonics of the SPB pulsations (Figure D3 in Appendix D). Another example is shown in the top panel of Figure D2 in Appendix D. Cases where frequencies in the β Cep range appear to be harmonics of SPB-range frequencies are noted with the flag *LOW_FREQ_HARMONICS*.

A similar type of impostor is the γ Doradus (γ Dor;

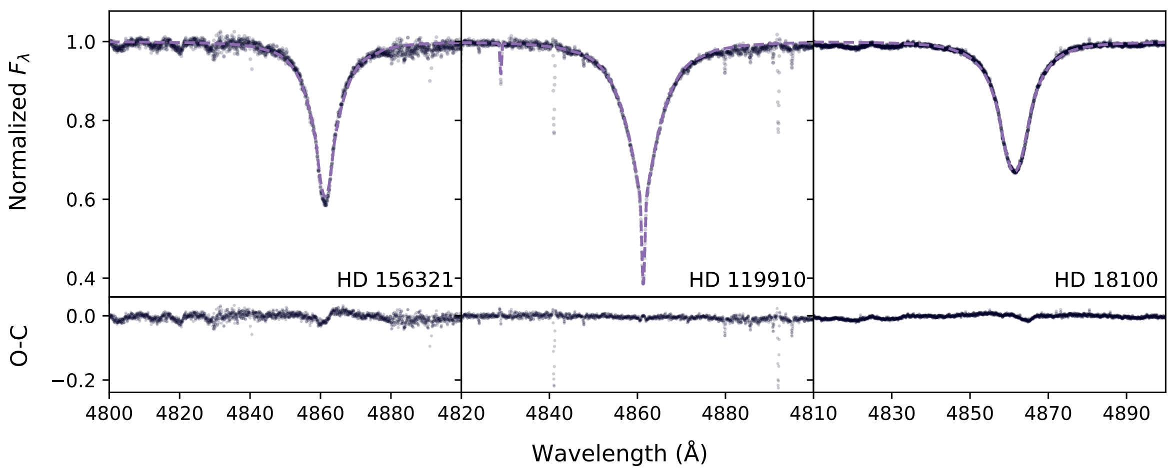

Figure 1. Top: Theoretical fits (dashed purple lines) to the observed $H\beta$ line profiles (solid gray lines) for three stars with different atmospheric parameters and $v \sin i$ values. Bottom: Residuals between the observed (O) and calculated (C) spectra.

GDOR) type pulsator. γ Dor stars are late A- to early F-type stars, with pulsation periods of ∼0.3–3 days. Without a clear spectral type, they can be confused with β Cep stars due to harmonics, similar to the case of SPB impostors (see the second panel from the top of Figure D2 in Appendix D). Cases where the target itself is identified as a possible GDOR pulsator are noted with the flag *GDOR*.

Another type of β Cep impostor is the class of δ Scuti (δ Sct; DSCT) stars, which are A- or F-type pulsators with pulsation periods of ∼0.5–7 hours that overlap with the β Cep period range. Reliable absolute magnitudes or spectral classifications generally distinguish DSCT from β Cep stars because of their substantially different luminosities or spectral types. However, incorrect cross-matches or blending may associate the detected variability with the wrong source, and a nearby DSCT star may contaminate the TESS light curve of a genuinely hot star. Therefore, DSCT variability can still cause an object to be mistaken for a β Cep candidate. The frequency spectrum can provide additional evidence, β Cep stars typically display a sparser frequency spectrum with only a few strong peaks, whereas δ Sct stars exhibit a denser spectrum with many independent modes and harmonics (see the third and fourth panels from the top of Figure D2 in Appendix D). Cases where the target is identified as a possible DSCT pulsator are noted with the flag *DSCT*; mentions explicitly attributed to a nearby, blended, secondary, or companion star are excluded from this flag and mentioned only in the notes.

In the visual classification we also check the effective temperature and spectral type when available. This makes it easier to identify impostors. Cases where Gaia ESP-HS $T_{\rm eff}$ values are inconsistent with the spectral types reported in the SIMBAD database are noted with the flag *SPEC_WRONG*.

5.2. *Classification Flags*

While performing the visual classification we are able to identify other phenomena visible in the light curve or the periodogram, on top of the pulsation type.

Stars whose light curves and periodograms do not show signs of significant variability are noted with the flag *CONST*.

We identify BCEP, Hybrid and SPB stars that also display stochastic low-frequency (SLF) variability, characterized by a broad power excess at low frequencies with no stable, coherent peaks, unlike κ-driven pulsations. Such cases are noted with the flag *SLF*. The physical origin of the SLF variability is uncertain without a more detailed study of these specific stars, but it may be associated with internal gravity waves which are stochastic buoyancy-driven oscillations (a discussion of SLF variability in O-B stars can be found in Thomson-Paressant et al. 2026). The *SLF* and *ONLY_SLF* categories are mutually exclusive: the former identifies SLF variability accompanying another variability classification, whereas the latter identifies stars displaying only SLF variability, without detected pulsation signals.

We also identify a subgroup of O–B stars previously classified as β Cep pulsators that, in the TESS data we analyze here, display only SLF variability, with no detected p- or g-mode pulsations. We note these stars with the flag *ONLY_SLF*.

We also identify stars displaying possible combination frequencies among their detected variability signals. We note these cases with the flag *COMB*.

Rotational modulation may arise from surface inhomogeneities such as chemical spots or magnetic features that co-rotate with the star, producing periodic variability at the rotation frequency and its harmonics. In the frequency spectrum, this typically appears as a low-frequency peak distinct from the pulsation modes. We note such cases with the flag *ROT_FLAG*.

We also identify three types of binary-related variability. Eclipsing binary (EB) systems are noted with the flag *EB*. Ellipsoidal variable (ELL) systems, in which tidal distortion produces brightness variations typically at twice the orbital frequency, are noted with the flag *ELL*. We note eccentric binary systems exhibiting the characteristic "heartbeat" variability around periastron with the flag *HEARTBEAT*.

5.2.1. *Photometric Quality Flags*

Because of the relatively low spatial resolution of TESS, contamination from nearby stars may affect the photometry. Suspected cases of blending are noted with the flag *BLEND_FLAG*. When the possible contaminating source is also included in the catalog and the origin of the detected variability is unclear, we include it in the Notes column and provide the TIC numbers of the relevant stars. We note such cases with the flag *NEARBY_STAR_FLAG*.

Noisy QLP photometry cases are noted with the flag *QLP_BAD*. We note cases where the photometry is affected by saturation-induced systematics for stars near the TESS saturation limit (~ 6 mag), with the flag *SAT*. For stars with both SPOC and QLP light curves, we generally prioritize the SPOC data. When the QLP light curve is of good quality and contains more TESS sectors than the SPOC light curve, we instead adopt the QLP data and note the star with the flag *QLP_OVER_SPOC*.

6. CLASSIFICATION RESULTS

We find a total of 1,130 β Cep stars, classified as BCEP ("pure β Cep"), Hybrid, BCEP+EB, and Hybrid+EB. We classify an additional 246 stars as candidates of these types. These stars, labeled as "Candidate", are those with TESS data of insufficient quality to confirm or reject a β Cep classification. Objects classified as BCEP+Candidate or Hybrid+Candidate (and their combinations with EB classifications) exhibit light-curve morphologies consistent with the assigned variability type, but lack ESP-HS effective temperatures and spectral-type information. The 122 stars without TESS light curves remain unclassified. Of stars reported as displaying or suspected to display β Cep pulsations, we reject 1,045 stars, with some of them classified as candidate SPB stars or flagged as DSCT/GDOR. We classify stars that are neither β Cep nor SPB candidates as "Non-BCEP" (these may include candidate DSCT or GDOR stars). We summarize the full classification results in Table 2. Of the 499 possible β Cep stars newly reported from our archival search, we classify 180 as confirmed β Cep stars, 18 as candidates, and 297 as rejected; the remaining four do not have TESS light curves and remain unclassified (see Section 2.2). The complete catalog, including the classifications, flags, and derived parameters, is provided electronically; Table E4 presents an excerpt.

Table 2. Results of the visual classification process, ordered by group size and separated into confirmed BCEP, candidates BCEP and non-BCEP groups.

Classification	Number of Stars	New
Hybrid	580	101
BCEP	457	64
BCEP+EB	80	12
Hybrid+EB	13	3
EB	60	7
Hybrid Candidate	60	5
Candidate	50	1
BCEP Candidate	47	5
BCEP+EB Candidate	26	0
Hybrid+EB Candidate	2	0
Candidate + EB	1	0
SPB Candidate	600	183
Non-BCEP	410	112
SPB+EB Candidate	28	2
EB+Non-BCEP	7	0
No TESS light curve	122	4

We identify 28 BCEP/Hybrid/+Candidate stars that display unusually large numbers of frequencies, sometimes 3 or 4 times more the typical number of dominant β Cep frequencies. We note these objects with the flag *MANY_FREQS*. We also identify 25 BCEP/Hybrid/+Candidate stars that display high frequencies ($>$ 15 c/d) that are not harmonics of lower-frequency signals. These objects are noted with the flag *HIGH_FREQS*. For some of these stars, we identify a possible contamination source nearby, while for others we identify no such source. Additional data might help determine the nature of the oscillation frequencies seen in these stars.

Table 3 presents the numbers of stars assigned each visual-classification flag (see Section 5) both across the entire catalog and among stars with confirmed or candidate β Cepclassifications and EB systems. We assign a value of 1 when we identify the corresponding phenomenon or data-quality issue with high confidence and a value of 0.5 when the identification is tentative. Individual stars may receive more than one flag.

The *Notes_classification* column in the catalog table provides additional information for individual stars. For objects classified as Candidate BCEP or Candidate, we specify the reason that we do not confirm the star as a β Cep pulsator and indicate possible alternative classifications, such as DSCT or GDOR. We also include notes on EB, ELL, heartbeat, and SLF variability.

7. STATISTICAL ANALYSIS

7.1. *Pulsation Parameters Choices*

We analyze the pulsation parameters of all stars classified as BCEP, Hybrid, and their combinations with EB systems, excluding candidate classifications. For each star, we apply the following hierarchy: when only SPOC data are available, we retain the SPOC entry; when only QLP data are available, we retain the entry only if it satisfies the quality criterion (QLP_BAD = 0). When both SPOC and QLP entries are present, we adopt the SPOC solution by default, except for a predefined subset of TICs for which the QLP solution is preferred because it includes a larger number of TESS sectors while still satisfying the quality criterion (QLP_BAD = 0). This procedure ensures that the analysis is based on high-quality light curves, since in some cases a light curve may be sufficient for visual classification but not adequate for quantitative frequency extraction. Here we use the frequency analysis results from the unbinned data (see Appendix F).

7.1.1. *Subsamples*

To determine the lower-frequency boundary for dominant β Cep pulsations, we manually inspect all BCEP and Hybrid stars with low dominant frequencies (all stars with dominant frequency below 4.5 $c\,d^{-1}$). We exclude cases in which the dominant low-frequency signal is attributable to SPB-like variability or to EB/ELL orbital modulation rather than to a β Cep p-mode. The lowest dominant frequency we retain as a β Cep pulsation is 3.28 $c\,d^{-1}$. From our inspection, frequencies below this threshold are generally associated with hybrid stars dominated by SPB-like variability, or systems where β Cep stars are part of EB or ELL configurations and the dominant variability is associated with orbital modulation rather than β Cep pulsation. Based on this inspection and the discussion presented in Section 7.2, we define Subsample *I* as stars with the dominant frequency $\geq 3.28\ c\,d^{-1}$.

We define Subsample *II* by stars with reliable Gaia astrometry using the Renormalized Unit Weight Error (RUWE), requiring RUWE < 1.4 (Luri et al. 2018), and parallaxes with high SNR, requiring *parallax_over_error* > 5 (Lindegren et al. 2021; Bailer-Jones 2015), for which the inferred distances are expected to be reliable.

For the parameters extracted directly from Gaia, namely effective temperature and surface gravity, as well as for the parameters derived in this work from Gaia quantities, including the solar-metallicity three-band luminosity (see Section 3.3), distance and M_G, M_{BP} and M_{RP}, which are the absolute Gaia magnitudes for the G, BP and RP bands (respectively) corrected for extinction, we examine stars from subsample *II*. For luminosity and the corrected absolute Gaia magnitudes, we additionally require Bayestar19 reddening estimates with both the *bayestar_converged* (a converged dust-map query) and *bayestar_reliable_dist* (a reliable queried distance) indicators set to true. For the pulsation constant Q, which depends on both Gaia-derived quantities and the pulsation frequencies, we examine stars that fall within the intersection of subsample *I* and *II*. For the dominant frequency and its corresponding amplitude, we examine stars from subsample *I*. For the V-band apparent magnitude, we examine the entire sample, since this information comes from SIMBAD, therefore not depending on the reliability of Gaia data or on frequency-based calculations. We list the subsample chosen for each parameter and the number of stars within it in Table 4.

7.2. *Distribution of Stellar and Pulsation Parameters*

We present the distributions of the main stellar and variability parameters for the different variability classes in Figure 2. For each parameter, we determine the histogram bins from the combined sample using the Freedman-Diaconis rule (Freedman & Diaconis 1981) and apply the same bin edges to all classifications. We calculate the KDEs using the `gaussian_kde` implementation in SciPy (Virtanen et al. 2020) and construct the ECDFs directly from the ordered parameter values.

The distributions presented here may reflect selection effects of the heterogeneous data sources used to construct the catalog. These sources rely on different telescopes, observing strategies, detection sensitivities, analysis techniques, and classification methods. We

Table 3. Numbers of secure and tentative visual-classification flag assignments.

Flag	Entire catalog		Confirmed + candidate β Cep	
	Secure (1)	Tentative (0.5)	Secure (1)	Tentative (0.5)
ROT	121	130	36	57
ELL	29	67	17	33
EB	15	18	10	15
HEARTBEAT	4	35	2	19
ONLY_SLF	0	45	0	5
SLF	47	141	14	104
DSCT	25	39	3	18
GDOR	6	6	1	0
CONST	21	17	2	3
QLP_BAD	179	12	164	7
SAT	8	7	7	6
SPEC_WRONG	36	20	33	15
BLEND	164	128	121	88
NEARBY_STAR	23	5	12	3
LOW_FREQ_HARMONICS	26	4	24	2
MANY_FREQS	32	17	28	0
HIGH_FREQS	34	16	25	0
COMB	21	3	1	1
QLP_OVER_SPOC	47	0	46	0

Note—Secure and tentative assignments correspond to flag values of 1 and 0.5, respectively. The final two columns include confirmed and candidate β Cep classifications, including their combinations with EB classifications.

Table 4. Subsample sizes and the parameters analyzed for each.

Parameter	Subsample *I*	Subsample *II*	Bayestar Quality	N_{BCEP}	N_{Hybrid}	$N_{\mathrm{BCEP+EB}}$	$N_{\mathrm{Hybrid+EB}}$
Distance (kpc)		V		329	454	51	9
Vmag				354	527	78	13
T_{eff} (K)		V		278	380	40	7
$\log g$		V		278	380	40	7
$\log(L/L_{\odot})$		V	V	120	159	11	4
Q (days)	V	V		125	135	3	3
M_G, M_{BP}, M_{RP} (mag)		V	V	143	185	16	5
f_1 (c/d)	V			342	421	22	6
A_1 (PPT)	V			342	421	22	6

Note—V in a column indicates which subsample is used for the statistical analysis of each parameter. Where V appears in both columns, the intersection of the two subsamples is used. For luminosity and the corrected Gaia absolute magnitudes, the Bayestar Quality selection additionally requires both Bayestar indicators to be true.

therefore cannot quantify or correct for these selection effects consistently, and we interpret the observed distributions as properties of the compiled sample rather than of the intrinsic Galactic β Cep population.

To compare the BCEP and Hybrid distributions quantitatively, we apply two-sample Kolmogorov–Smirnov (KS) tests using `ks_2samp` from SciPy (Virtanen et al. 2020) and report the raw p-value for each parameter. We additionally report p-values adjusted using the Benjamini–Hochberg procedure (Benjamini & Hochberg 1995) in Appendix G.

We fit one- and two-component Gaussian-mixture models using the `GaussianMixture` implementation in scikit-learn (Pedregosa et al. 2011) and compare the models using the BIC. A preference for two components may indicate internal structure, but does not by itself establish bimodality because it may also result from skewness or extended tails. We also examine kernel density estimates (KDEs) and empirical cumulative distribution functions (ECDFs), which we present in Figures G5 and G6 in Appendix G, respectively. We present the complete set of values from the statistical tests in Table G7 in Appendix G. We restrict the quantitative comparison to the BCEP and Hybrid classes because the corresponding samples of stars in eclipsing-binary systems are substantially smaller. We therefore discuss the EB distributions only descriptively.

The dominant-frequency distributions of the BCEP and Hybrid classes are broadly similar, although the Hybrid distribution is shifted toward somewhat higher frequencies and shows a possible bimodal structure. The BCEP frequencies span 3.28–16.63 $c\,d^{-1}$, with a median of 5.84 $c\,d^{-1}$ and a highest-bin center of 5.08 $c\,d^{-1}$. The Hybrid frequencies span 3.31–16.71 $c\,d^{-1}$, with a median of 6.32 $c\,d^{-1}$ and highest-bin center at 6.12 $c\,d^{-1}$. Across all four populations, the frequencies span 3.28–16.71 $c\,d^{-1}$, with a median of 6.11 $c\,d^{-1}$. The ECDFs and the KS result support the observed shift between the BCEP and Hybrid distributions. The BIC strongly favors a two-component Gaussian model for both classifications, with $\Delta BIC = 142.58$ for BCEP and $\Delta BIC = 95.68$ for Hybrid. The KDEs similarly show broad, asymmetric distributions with a weaker secondary peak in both classifications. We therefore conclude that the frequency distributions contain internal structure and show possible bimodality, although the secondary populations are substantially smaller than the primary populations.

The amplitude distributions indicate that the pure β Cep stars tend to reach higher amplitudes than the Hybrid stars, as is particularly evident from the extended high-amplitude tail of the BCEP distribution. The BCEP amplitudes span 0.14–135.58 PPT, with a median of 11.51 PPT, whereas the Hybrid amplitudes span 0.07–54.81 PPT, with a median of 7.11 PPT. Both distributions have the same highest-bin center of 5.62 PPT, indicating that their main difference lies in the higher median and more extended high-amplitude tail of the BCEP distribution. Across all four populations, the amplitudes span 0.07–135.58 PPT, with a median of 8.70 PPT. This difference is also visible in the ECDFs and is supported by the KS result. Although the BIC strongly favors two Gaussian components for both classifications, the KDEs show strongly asymmetric distributions rather than a clear bimodal structure.

Manual inspection further shows that, when the dominant variability of a Hybrid star lies in the SPB g-mode regime, the amplitudes of its β Cep p-mode frequencies are typically lower than the amplitude of the dominant g-mode variability.

The BCEP stars in EB systems also tend to have lower amplitudes than the apparently single BCEP stars. No corresponding tendency is apparent for the Hybrid stars in EB systems. Because these EB subsamples contain relatively few stars, these comparisons are descriptive. Several effects may contribute to this behavior. First, flux dilution by the companion can reduce the observed pulsation amplitudes. Another possible explanation is related to the viewing geometry of EB systems, which are observed at high orbital inclinations, with the orbital plane viewed nearly edge-on ($i \simeq 90°$). If the pulsation geometry of the star is aligned, or approximately aligned, with the orbital-angular-momentum axis, this would imply that the star is also viewed nearly equator-on. In such a geometry, geometrical cancellation of non-radial axisymmetric modes ($m = 0$) can be stronger, leading to lower observed pulsation amplitudes. Moreover, in close binaries, tidal effects and/or past binary interaction may modify the intrinsic pulsation properties and the observed mode amplitudes; depending on the system configuration, such effects could either enhance specific modes or contribute to lower amplitudes. In addition, these systems often show more complex frequency spectra, which may make frequency extraction more difficult.

The distance distributions overlap substantially, with BCEP stars tending toward slightly larger distances than Hybrid stars. The Hybrid histogram shows a main peak near 2 kpc and possible additional peaks near 0.5 kpc and 3–4 kpc. The BCEP distances span 0.28–9.08 kpc, with a median of 2.39 kpc and a highest-bin center of 2.38 kpc. The Hybrid distances span 0.15–8.67 kpc, with a median of 2.21 kpc and a highest-bin center of 1.91 kpc. Across all four populations, the distances span 0.15–9.08 kpc, with a median of 2.31 kpc. The

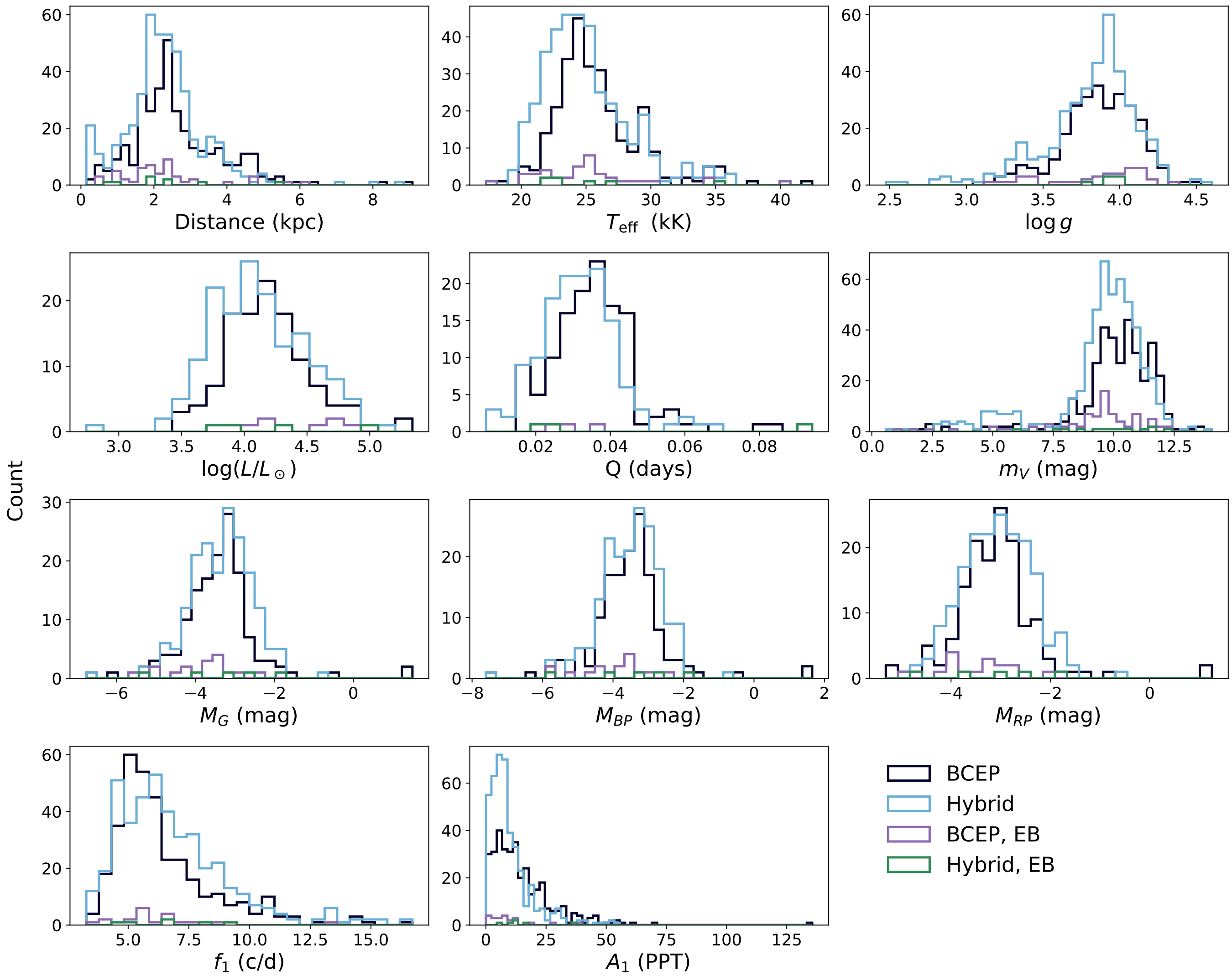

Figure 2. Distributions of key stellar and variability parameters for the different variability classes. M_G, M_{BP} and M_{RP} are the absolute Gaia magnitudes in the G, BP and RP bands (respectively) corrected for reddening and m_V is the apparent magnitude from SIMBAD. Q stands for the pulsation constant, while f_1 denotes the dominant frequency and A_1 its corresponding amplitude.

ECDFs and KS tests support a difference between the BCEP and Hybrid distributions. The BIC strongly favors two Gaussian components for both classifications, with $\Delta BIC = 31.26$ for BCEP and $\Delta\text{BIC} = 38.31$ for Hybrid.

The apparent V-band magnitude distributions show that the Hybrid distribution is shifted toward brighter apparent magnitudes than the BCEP distribution, with both distributions showing some evidence of bimodality. The BCEP values span 1.25–13.66 mag, with a median of 10.26 mag and a highest-bin center of 10.61 mag, whereas the Hybrid values span 0.58–14.06 mag, with a median of 9.83 mag and a highest-bin center of 9.62 mag. Across all four populations, the values span 0.58–14.06 mag, with a median of 9.96 mag. The shift of the Hybrid distribution towards brighter apparent magnitudes is also visible in the ECDFs and is supported by the KS result. The BIC strongly favors two Gaussian components for both classifications, supporting internal structure in the distribution. However, the KDEs suggest asymmetric distributions with extended bright tails rather than two clearly separated populations. Moreover, because m_V depends on distance, extinction, and catalog-selection effects, the observed difference cannot be interpreted directly as an intrinsic luminosity difference.

The absolute Gaia magnitudes for the G, BP and RP bands corrected for reddening also show broadly similar distributions by classification type. The absolute magnitudes in the BP band extend to brighter magnitudes than those in the G and RP bands, as expected for OB-type stars. For M_G, the BCEP distribution spans −6.76–1.50 mag, with a median of −3.46 mag and a highest-bin center of −3.17 mag. The Hybrid distribution spans −6.63––0.73 mag, with a median of −3.29 mag and a highest-bin center of −3.17 mag. Across all four populations, the M_G, M_{BP}, and M_{RP} values span −6.76–1.50, −7.60–1.65, and −5.31–1.25 mag, respectively, with corresponding medians of −3.37, −3.49, and −3.11 mag. For M_{BP}, the BCEP and Hybrid distributions span −7.50–1.65 mag and −7.60––0.78 mag, respectively. Their medians are −3.54 and −3.42 mag, and both have a highest-bin center of −3.26 mag. For M_{RP}, the corresponding ranges are −5.31–1.25 mag and −4.92––0.55 mag, with medians of −3.11 and −3.05 mag. Both M_{RP} distributions have a highest-bin center of −3.00 mag. The statistical tests support the visible similarity between the BCEP and Hybrid distributions in all three bands. The BIC favors two components for BCEP distributions in all three bands, but not for the Hybrid distributions. The KDEs do not show distinct secondary peaks, indicating that the BIC preference for two components in the BCEP distributions may reflect a small number of unusually bright stars rather than two separate populations.

The effective temperature distributions overlap substantially, with both classifications sharing a main peak near 24 kK. However, the BCEP distribution is shifted toward slightly higher temperatures and extends to higher values. The BCEP temperatures span 18.91–42.45 kK, with a median of 25.29 kK and a highest-bin center of 24.41 kK, whereas the Hybrid temperatures span 17.29–36.26 kK, with a median of 24.44 kK and an average of the tied highest-bin centers of 24.00 kK. Across all four populations, the temperatures span 17.29–42.45 kK, with a median of 24.76 kK. The ECDFs and the KS result support a difference between the complete distributions despite sharing a main peak near 24 kK. The BIC favors a two-component model for both classifications, with $\Delta BIC = 54.66$ for BCEP and $\Delta BIC = 45.00$ for Hybrid. The KDEs show a dominant temperature peak accompanied by weaker shoulders or extended tails. We therefore interpret the temperature distributions as having some internal structure.

The $\log g$ distributions of the BCEP and Hybrid stars overlap substantially. The BCEP distribution shows a single main peak, whereas the Hybrid distribution shows a lower-gravity tail and possible bimodal structure. The BCEP values span 3.11–4.49, with a median of 3.89 and a highest-bin center of 3.86. The Hybrid values span 2.47–4.60, with a median of 3.86 and highest-bin center of 3.93. Across all four populations, the values span 2.47–4.60, with a median of 3.88. The KDEs and ECDFs show substantial overlap between the BCEP and Hybrid distributions, and the KS test does not indicate a clear overall difference between these classes. Separately, the BIC strongly favors a two-component model within the Hybrid distribution ($\Delta BIC = 50.64$), supporting the possible bimodal structure seen in its histogram.

Table 5. Confirmed β Cep stars with Gaia ESP-HS surface gravities below $\log g = 3.2$, listed in order of increasing $\log g$.

TIC	Classification	$\log g$	$\sigma_{\log g}$
139385056	Hybrid	2.474	0.622
29277573	Hybrid	2.588	0.511
209036736	Hybrid	2.763	0.030
232846315	Hybrid	2.815	0.009
378726058	Hybrid	2.869	0.655
400902778	Hybrid	2.886	0.014
34803944	Hybrid	2.892	0.015
372674359	Hybrid	2.952	0.018
390098366	Hybrid	2.998	0.009
295435513	Hybrid	3.018	0.021
330241794	Hybrid	3.109	0.024
251637508	BCEP	3.109	0.023
321947833	BCEP, EB	3.114	0.013
458831281	Hybrid	3.131	0.029
348023621	Hybrid	3.153	0.007
442170794	Hybrid	3.167	0.027
155530282	BCEP	3.175	0.030
120859681	Hybrid	3.181	0.026
348506748	BCEP	3.193	0.011
465555235	BCEP	3.195	0.031

Twenty stars have ESP-HS surface gravities below $\log g = 3.2$. 15 are Hybrid stars, four are BCEP stars and one is a BCEP in EB system. Brott et al. (2011) identify an empirical transition near $\log g = 3.2$, which they interpret as the end of the main sequence for stars with masses of approximately 10–20 $M_\odot$. Therefore, these stars may have evolved beyond the main sequence. We list them in Table 5. However, several of the lowest-gravity values have comparatively large reported uncertainties, so we interpret their evolutionary status cautiously. Spectroscopic follow-up is required to verify their surface gravities and evolutionary states.

For $\log(L/L_\odot)$, the Hybrid distribution tends toward lower values than the BCEP distribution. This can also be seen in the presence of some Hybrid stars in the lower-right region of the HR diagram of the catalog (see Section 7.4). The BCEP luminosities span 3.45–5.34, with a median of 4.19 and a highest-bin center of 4.18. The Hybrid luminosities span 2.74–5.15, with a median of 4.08 and a highest-bin center of 4.04. Across all four populations, the luminosities span 2.74–5.34, with a median of 4.13. The statistical tests, however, do not support the tendency of the Hybrid distribution to lower luminosities. We therefore regard the lower luminosities of the Hybrid stars as a descriptive tendency visible in the distribution, rather than as a clear separation between the two classifications.

Finally, the distribution of the pulsation constant Q shows a more extended low-Q tail for the Hybrid class, whereas the BCEP distribution extends to higher Q values. The BCEP values span 0.015–0.084 d, with a median of 0.035 d and a highest-bin center of 0.036 d. The Hybrid values span 0.007–0.067 d, with a median of 0.032 d and a highest-bin center of 0.036 d. Across all four populations, the values span 0.007–0.094 d, with a median of 0.033 d. The inferred values remain within the expected range for p-mode pulsators. The shift and the broader low-Q tail are visible in the KDEs and ECDFs, while the KS result supports a difference between the distributions.

We summarize the ranges, medians, and highest-bin centers for each parameter and classification in Table G6 in Appendix G.

7.3. *Comparison Between Spectroscopic Parameters and Gaia Parameters*

We compare the spectroscopically derived $T_{\rm eff}$ and $\log g$ values with the corresponding Gaia parameters (Gaia Collaboration et al. 2023b), and present our results in Figure 3. The differences between the spectroscopic and Gaia-derived parameters become increasingly negative toward higher $T_{\rm eff}$ and higher $\log g$ values. We note, however, that a few outlying points, particularly in the $T_{\rm eff}$ comparison, may influence the apparent trends, and we therefore interpret them with caution. Given that the ESP-HS pipeline is specifically designed for hot stars, we expect its results to show better agreement with our spectroscopic measurements than those obtained from the Gaia GSP-Phot pipeline. The GSP-Phot pipeline is not specifically optimized for hot stars, and the limited temperature sensitivity of its low-resolution BP/RP spectra results in a strong degeneracy between effective temperature and extinction. This degeneracy may introduce systematic errors in both parameters and thereby contribute to the observed discrepancies (Fouesneau et al. 2023). We do not observe a clear improvement in the agreement for the stars in our

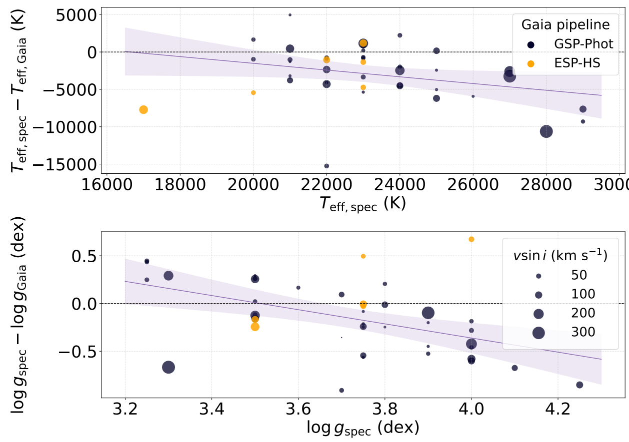

Figure 3. Comparison between the spectroscopically derived atmospheric parameters and the corresponding Gaia values for the studied stars. The upper and lower panels show the differences in $T_{\rm eff}$ and $\log g$, respectively, as functions of the corresponding spectroscopic values. The solid purple lines represent linear fits to the distributions in the upper and lower panels, while the shaded regions correspond to the 95% confidence intervals of those fits. The size of each symbol is scaled according to the $v\sin i$ with larger symbols indicating more rapidly rotating stars. Orange points indicate differences calculated using Gaia ESP-HS parameters, whereas dark gray points indicate differences calculated using Gaia GSP-Phot parameters.

sample. However, only six stars from our sample have ESP-HS measurements available, which limits our ability to make a meaningful comparison between the two Gaia pipelines. A sample with more ESP-HS measurements is required to assess their relative performance more robustly.

In Figure 4, we present the distributions of the stellar parameters derived from the SALT spectra collected in this work. We plot 55 stars, excluding stars that we reclassify in this work as non-β Cep pulsators, stars that display spectral features potentially originating from another object (see Section 4), and stars that we do not reclassify because they do not have TESS light curves.

The effective-temperature distribution spans 17,000–23,000 K. The lowest temperatures, 17,000 K for HD 145794 and HD 149100, are lower than expected for β Cep stars, but still possible within 1,000 K error.

The temperature range obtained from the Gaia data is ∼17,290–42,450 K. Moreover, the identification of late O-type β Cep pulsators in the previous section, together with Gaia temperatures reaching up to 42,450 K, suggests that the upper limit derived from the SALT sample does not reflect the full temperature range of the β Cep population, but rather the limited size of the spectroscopic sample.

The surface gravity distribution spans 3.25–4.25, whereas the Gaia values of the full sample range between approximately 2.47 and 4.60. The values derived from the SALT sample fall within this range and are therefore also consistent with the Gaia results. The projected rotational velocities range from 3 to 324 km/s.

7.4. *Positions on the HR Diagram*

Figure 5 presents the HR diagram of the confirmed β Cep pulsators in our catalog. The left panel shows 323 confirmed β Cep stars with Gaia ESP-HS effective temperatures and weighted three-band Bayestar bolometric luminosities assuming solar metallicity (see Section 3.3). The right panel shows an extended sample of 783 confirmed β Cep stars, using the same ESP-HS temperatures and G-only luminosities calculated from Gaia ESP-HS A_G values assuming solar metallicity. A G-only Bayestar luminosity would retain the same 323 stars as the weighted three-band method. In contrast, the G-only ESP-HS-A_G method includes all 323 stars in the Bayestar sample and 460 additional stars; the comparison and resulting luminosity choices are described in Appendix B. For the stars common to both samples, we use the dispersion between the G-only and three-band luminosities to estimate the additional uncertainty of the single-band method, and add this empirical scatter in quadrature to the G-only luminosity uncertainties. The larger typical error cross in the right panel reflects this additional uncertainty.

We also plot solar-metallicity stellar tracks from the β Cep grid of Vanrespaille et al. (2026) for five different masses (7.00, 10.23, 14.96, 21.88, and 29.85 $M_\odot$), spanning the full mass range of the grid. For each mass, we show models computed with both the minimum and maximum mixing values included in the grid: $\log(D) = 1$, $f_{ov} = 0.005$ and $\log(D) = 5$, $f_{ov} = 0.035$, respectively. Here, D denotes the diffusion coefficient (in $\mathrm{cm^2 s^{-1}}$), and f_{ov} is the dimensionless overshooting parameter expressed in units of the pressure scale height. Additionally, the instability regions for p-modes and g-modes are shown.

Most β Cep stars are concentrated in the mass range of 7–15 $M_\odot$, with only a few objects extending towards lower or higher masses. Most of the stars located below the lower boundary of the region of overlapping p- and g-mode instability, as well as those in the region where only g-modes are expected to be unstable, are hybrid stars or hybrids in EB systems. However, these regions are not exclusively occupied by Hybrid stars and a few "pure" β Ceppulsators also lie outside the displayed instability regions as well. The extended sample shows the same overall temperature–luminosity distribution, while revealing additional lower luminosity stars and a broader luminosity distribution. This broader spread is somewhat expected because its luminosities are derived from one Gaia band rather than from the weighted three-band Bayestar calculation.

In Figure 6, we display the Gaia color-magnitude diagram for 761 confirmed β Cep stars with available Gaia DR3 ESP-HS extinction and reddening values, overlaid on the upper-left edge of the Gaia Catalog of Nearby Stars (GCNS; Gaia Collaboration et al. 2021). We retain only stars with reliable Gaia astrometry, defined as RUWE < 1.4 and *parallax_over_error* > 5. When Gaia DR3 ESP-HS extinction and reddening parameters are available, we directly adopt the values provided by the pipeline. Otherwise, we obtain reddening estimates from the Bayestar19 three-dimensional dust map (Green et al. 2019) using the *dustmaps* Python package (Green 2018). We convert these estimates to extinction in the Gaia bands using the coefficients of Pedersen et al. (2020), based on the Fitzpatrick (2004) reddening law. For the BP band, we adopt the mean of the bright- and faint-passband coefficients reported by Pedersen et al. (2020). We exclude stars with extinction-corrected colors $(BP - RP)_0 < -0.521$, because these values are bluer than the approximate physical limit for stellar colors and result from extinction or reddening corrections that are too large relative to their observed colors. This removes 22 stars from the ESP-HS sample. The catalog stars occupy the blue, luminous upper-main-sequence region expected for β Cep pulsators, with substantial overlap between the BCEP and Hybrid populations.

7.5. *Spectral Types*

Most of the spectral classifications in our catalog come from the SIMBAD database, which compiles classifications from different literature sources. Some of these spectral classifications are inconsistent with the corresponding ESP-HS effective temperatures. For example, V1155 Cas, is classified as B5 but has an ESP-HS effective temperature of 29,455.61 K.

To determine which published spectral classifications are sufficiently reliable for constructing the spectral-type distribution of the β Cep stars, we test their consistency with the Gaia ESP-HS effective temperatures. We perform this test using reference spectral-type–effective-temperature relations constructed from modern non-LTE analyses of O- and B-type stars. We do not use the ESP-HS temperatures to infer or assign new spectral types.

For O-type stars, we adopt the mean effective temperature for each spectral subtype and luminosity class listed in Table D2 of Holgado et al. (2025). For early- and mid-B dwarfs and giants, we associate the spec-

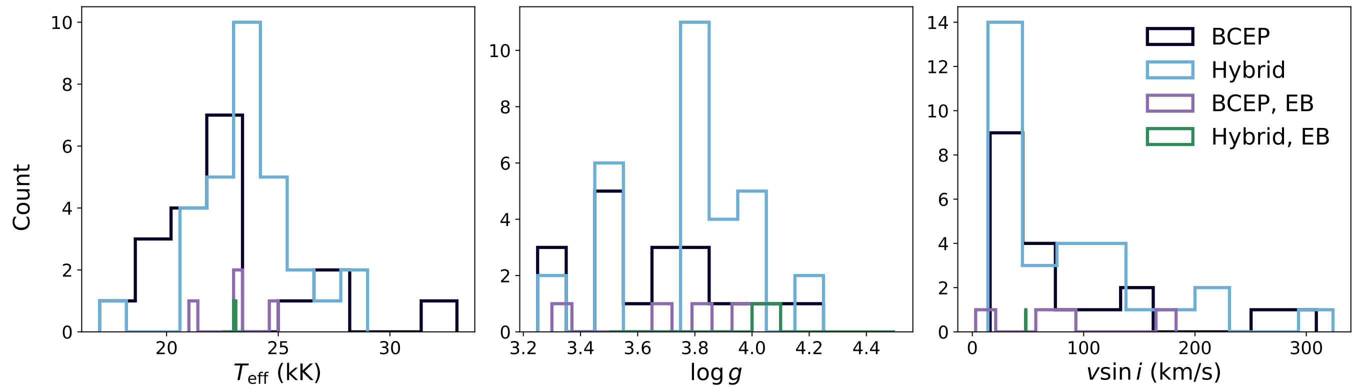

Figure 4. Same as Figure 2 but for the stellar parameters derived from the SALT spectra collected in this work classified as β Cep stars.

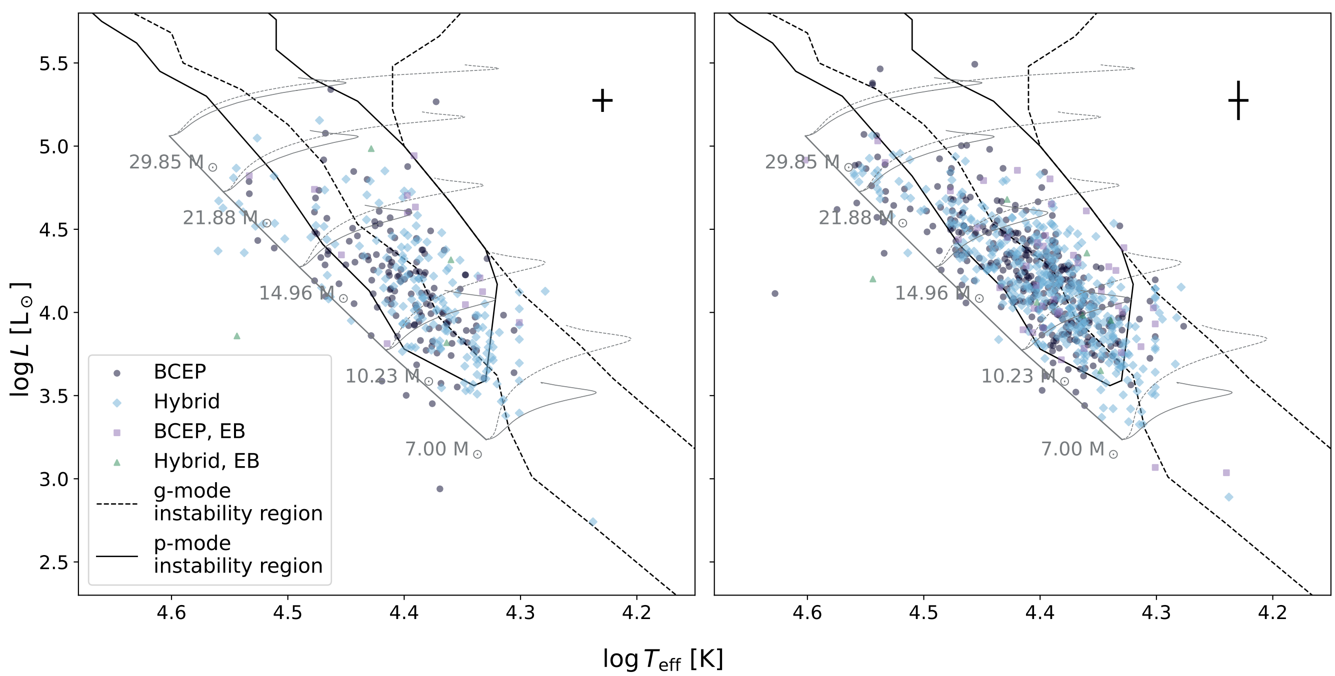

Figure 5. HR diagram for the confirmed β Cep stars. The left panel shows 323 stars with Gaia ESP-HS effective temperatures and weighted three-band Bayestar luminosities calculated assuming solar metallicity. The right panel shows 783 stars with Gaia ESP-HS effective temperatures and G-only luminosities calculated using the Gaia ESP-HS A_G values and assuming solar metallicity. Grey lines show stellar tracks from Vanrespaille et al. (2026) for five different masses as noted (solid lines represent tracks with minimum mixing and dashed lines represent tracks with maximum mixing as included in the grid). The p- and g-mode instability regions, adopted from Burssens et al. (2020), are shown within the black solid and dashed lines, respectively. The black crosses show the median propagated uncertainties in each panel.

tral classifications listed in Table 1 of Nieva & Przybilla (2012) with the effective temperatures derived for the same stars in their Table 5. We then group these stars by spectral subtype and luminosity class and calculate the mean effective temperature of each group. We apply the same grouping and averaging procedure to the B-type supergiants with atmospheric parameters listed in Table 3 of Markova & Puls (2008). Together, these values form the reference spectral-type–effective-temperature relations used in our consistency test.

Before performing the consistency test, we standardize the published spectral classifications. We ignore suffixes (e.g., n for rotational broadening, e for emission lines, and p for peculiar spectral features). We exclude binary systems with multiple spectral types. We also do not include ambiguous classifications such as “O” or “OB”. We then decompose each valid spectral type into three parts: the spectral class (O or B), the numerical subtype

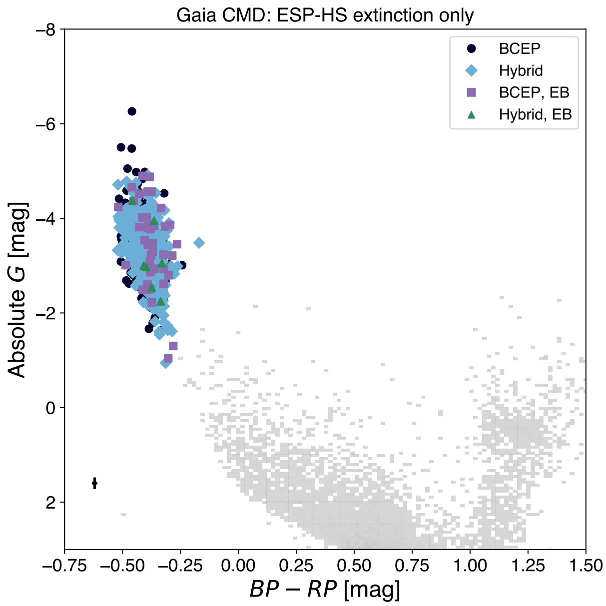

Figure 6. Gaia color-magnitude diagram for the extinction- and reddening-corrected stars in the catalog. The black cross in the bottom-left region shows the mean propagated uncertainty, including the Gaia photometric, parallax, and ESP-HS extinction or reddening uncertainties. The upper-left boundary of the GCNS sample is shown in grey.

and the luminosity class.

For each star, we test whether its ESP-HS effective temperature is consistent with its published spectral subtype. Because the published subtype and luminosity class may be uncertain, we consider all calibration entries for reference subtypes within ±1.5 subtype numbers and include all available luminosity classes. For example, for a star classified as B2, we examine the calibrated temperatures for subtypes B0.5–B3.5 across all available luminosity classes. We define the acceptance interval from the minimum and maximum calibrated mean effective temperatures among all these entries and extend it by 1500 K at both ends:

$$T_{\rm min} = \min(T_{\rm eff,mean}) - 1500\,{\rm K}$$

$$T_{\rm max} = \max(T_{\rm eff,mean}) + 1500\,{\rm K}.$$

We consider the spectral classification consistent with the ESP-HS temperature if the latter falls within this interval.

The consistency test includes 545 stars, of which 433 have ESP-HS temperatures consistent with their published spectral classifications under these criteria.

We present the stacked distribution of the matched spectral types in Figure 7. The spectral types that pass the consistency test span O9–B3. Most β Cep stars have spectral types B1 or B2, consistent with Stankov & Handler 2005. The most common luminosity class is V, as expected for β Cep stars, which are primarily main-sequence (MS) stars. However, the sample also includes subgiants (IV), giants (III), bright giants (II) and supergiants (I). We do not consider this finding concerning because luminosity classes should be seen as statistical relationships with absolute magnitude that exhibit large scatter (Jaschek & Gomez 1998).

Among the stars for which we collect SALT spectra (Table C2 in Appendix C), the star with the earliest spectral type and a corresponding effective temperature consistent with its spectral classification is HD 156172, an O9V star. The stars with the latest spectral types and corresponding effective temperatures consistent with their spectral classifications are of spectral type B2. The resulting O9–B2 range fits well within the O9–B3 range obtained from the consistency test.

The temperature range inferred from the temperature distribution shown in Section 7.2 is ∼17,290–42,450 K, which corresponds to spectral types O5–B3. This range encompasses the O9–B2 spectral-type range identified from the SALT spectra and is broadly consistent with the O9–B3 range obtained from the spectral-type matching analysis. However, the temperature distribution suggests that the population may extend to earlier spectral types, potentially reaching O5.

7.6. *Coordinates and Velocities*

Figure 8 displays the Galactic coordinates of the 1,130 confirmed β Cep stars. We use Gaia coordinates for 1,121 stars and SIMBAD coordinates for the remaining nine stars, which lack Gaia coordinates. Most of the stars are distributed along the Galactic plane, as expected, with some scatter around it.

In Figure 9 we present the tangential velocity vectors for the astrometry qualified (RUWE < 1.4, and *parallax_over_error* > 5) 932 subset of confirmed β Cep stars in the right ascension (RA) and declination (Dec) plane. We compute these velocities from the Gaia DR3 proper motion components and parallax based distances. We restrict the sample to stars with reliable Gaia astrometry by requiring RUWE < 1.4 and *parallax_over_error* > 5. The vectors exhibit a coherent large-scale pattern, while some stars show clear deviations.

Some stars have substantially larger tangential velocities or directions that deviate more strongly from the Galactic plane. We identify 16 stars with exceptional tangential velocities, defined as values exceeding three standard deviations above the sample median (183.51 $km; s^{-1}$). We additionally identify 39 stars with

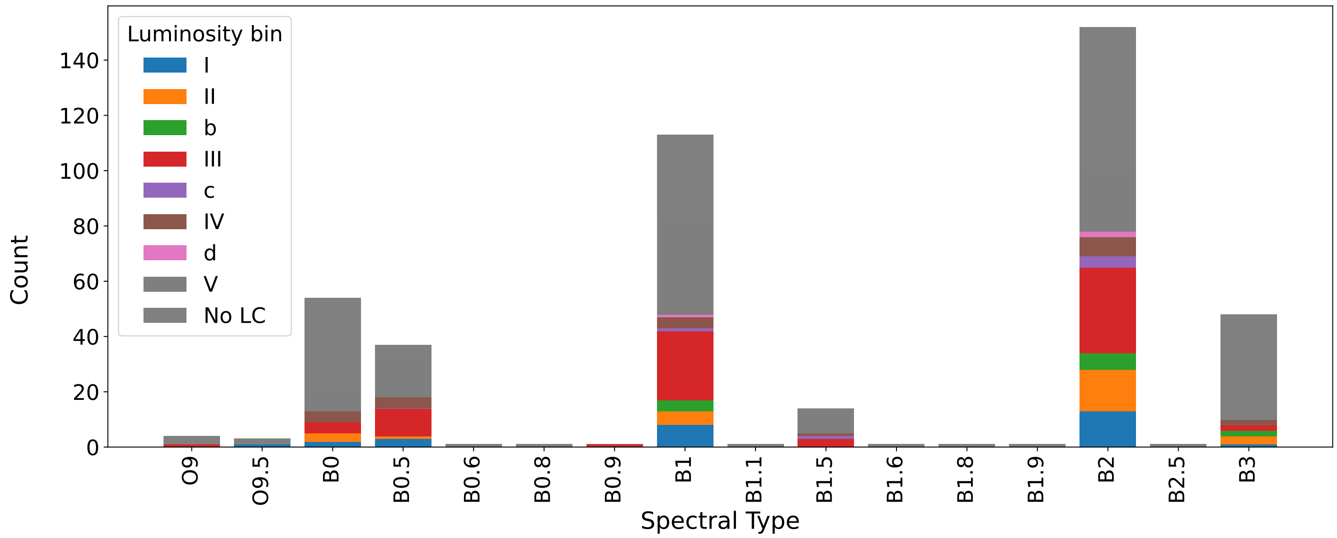

Figure 7. Distribution of the matched spectral types for the confirmed β Cep stars in the catalog. The distribution is stacked by reported luminosity class (I–V and intermediate classes), with stars lacking a reported luminosity class shown in grey.

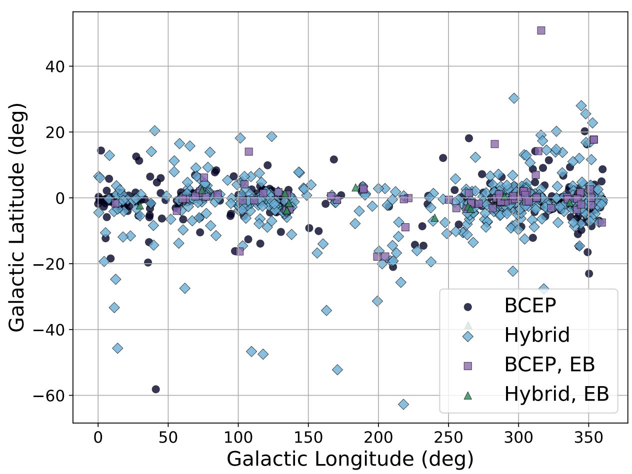

Figure 8. Galactic coordinates of the 1,130 confirmed β Cep stars.

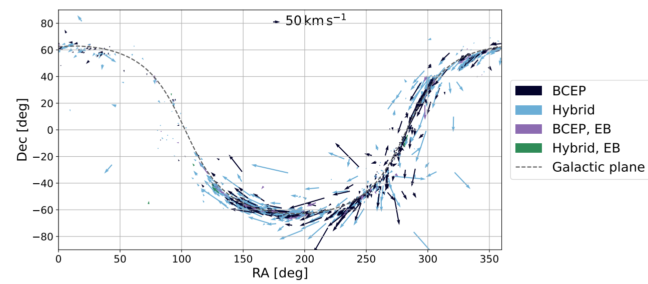

Figure 9. Tangential velocity vectors of 932 confirmed β Cep stars in the catalog in the RA and Dec directions. The dashed curve marks the Galactic plane.

directional deviations exceeding three standard deviations (46.30°) and tangential velocities greater than 20 $km; s^{-1}$. We adopt the latter velocity limit after visually examining the stars with exceptional directions, in order to exclude objects whose large directional angles result from very small velocity components parallel to the Galactic plane despite their low total tangential velocities. We list these stars in Table H8 in Appendix H. These selections identify empirical outliers within our catalog; because we do not correct the velocities for Galactic rotation or Solar motion, we do not interpret them as confirmed departures from a Galactic-kinematic model or as confirmed runaway stars. However, these stars may be interesting targets for future investigation.

In Figure 10 we present the distributions of proper motion, tangential velocity, and space velocity for the stars in our catalog. We convert the Gaia DR3 proper motion measurements into physical plane-of-sky velocities using the parallax based distances. We compute the space velocities as the norm of the tangential and radial velocity components when radial velocities are available. Consequently, the space-velocity panel contains only 127 stars, compared with 932 stars in the proper-motion and tangential-velocity panels.

For the proper-motion and tangential-velocity distributions in Figure 10, both the BCEP and Hybrid classes show internal structure consistent with bimodality. The KDEs in Figure H7 in Appendix H similarly show two broad components. The BIC strongly favors two components for the BCEP proper-motion and tangential-velocity distributions (ΔBIC $= 51.10$ and 25.22, respectively) and for the corresponding Hybrid distributions (ΔBIC $= 28.18$ and 38.03, respectively). Most of the stars with radial-velocity measurements have heliocentric space velocities below approximately $(150, \mathrm{km}, \mathrm{s}^{-1})$,

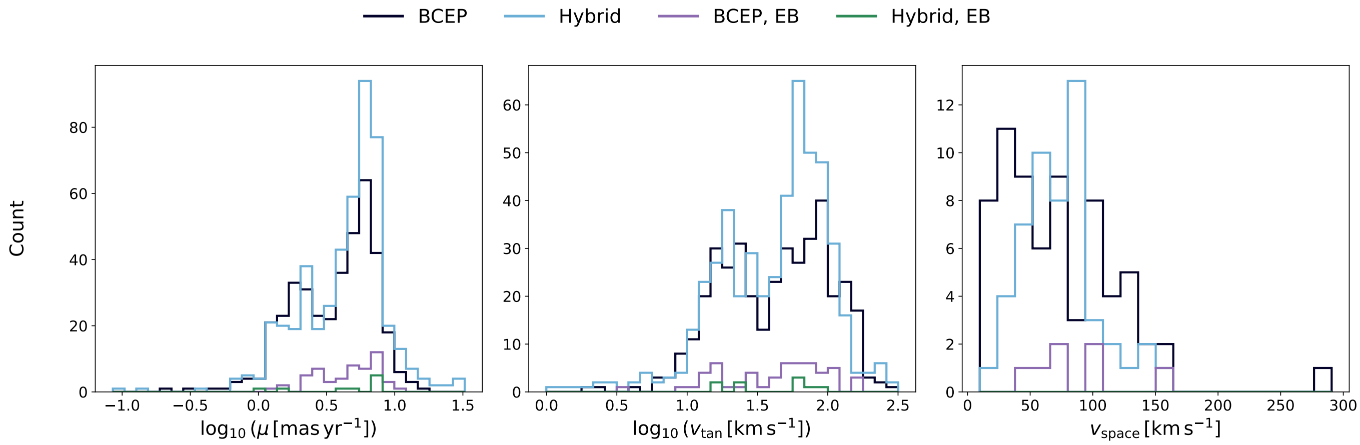

Figure 10. Distributions of proper motion (left), tangential velocity (middle), and total space velocity (right) for the confirmed β Cep stars with reliable Gaia astrometry. The colors identify the different classifications. The space-velocity panel includes only stars with available radial-velocity measurements.

while a small number reach higher velocities. Because we do not correct these velocities for Galactic rotation or Solar motion, we do not interpret the high-velocity objects as confirmed runaway stars.

8. SUMMARY

We collect 2,543 candidate β Cep stars from the literature and from analysis of archival data (Section 2). Of these, 2,421 have TESS data and 2,526 have Gaia data. Based on the TESS light curves, we perform frequency analysis (Section 3.2) and visually classify each star (Section 5). We confirm 1,130 of these candidates as β Cep stars (Section 6), of which 180 are newly reported here. The confirmed sample includes 593 hybrid stars, displaying both β Cep and SPB pulsations, and 537 "pure" β Cep pulsators. Across these confirmed classes, 93 stars show clear EB signatures in their light curves and/or periodograms. In addition to these 1,130 confirmed stars, we classify 246 stars as candidate β Cep / hybrid or EB systems because of noisy light curves that prevent a definitive classification or a lack of reliable spectral or temperature information; 18 of these stars are newly reported here.

We find β Cep and hybrid stars within ELL and heartbeat systems, and detect signs of rotational modulation (Table 3). We also find stars with SLF variability on top of their pulsation signals, as well as stars that display only SLF variability with no detected pulsation signal. We further identify 28 β Cep stars that display three to four times more frequencies than typically observed in this class, along with 25 stars that, in addition to their β Cep pulsations, display high frequencies (greater than 15 c/d) that are not harmonics of lower frequencies. We discuss the possibility that these signals arise from contamination by nearby stars given the TESS spatial resolution. We indeed identify a candidate contamination source for some of these stars, but the rest require further investigation.

We also collect spectra for 67 selected southern-hemisphere β Cep candidates based on their ranking according to the number of pulsation modes detected from the ground, their observability with TESS and their apparent magnitude. We analyze and model these spectra to derive effective temperature, surface gravity, and projected rotational velocity. We compare the effective temperatures and surface gravities with the values estimated by Gaia. The differences between the spectroscopically and Gaia-derived parameters become increasingly negative toward higher $T_{\rm eff}$ and higher $\log g$, although a few outliers may influence these apparent trends. The limited number of stars with ESP-HS measurements prevents a robust comparison between the Gaia pipelines and the parameters derived from the spectra.

We perform a statistical study (Section 7) of the 1,130 confirmed β Cep stars. The dominant frequencies of stars classified as "pure" β Cep and hybrid stars span 3.28–16.63 and 3.31–16.71 c/d, respectively, with medians of 5.84 and 6.32 c/d. We interpret these distributions with caution because of possible selection effects discussed in Section 7.2. We classify 246 additional stars as candidate β Cep/hybrid or EB systems and 1,045 stars as candidate SPB, DSCT, GDOR, or unknown-variability-type objects, or as stars without a detectable pulsation signal in the available TESS data.

For our sample, we find that cadence equalization has a negligible effect on the recovered dominant frequencies, while the amplitudes agree exactly for 62.1% of the stars. When differences occur, the amplitudes derived from the unbinned data tend to be slightly larger. We adopt the unbinned data for the statistical analysis because they preserve the original amplitude distribution. See Appendix F for a complete discussion.

We find that β Cep stars span the spectral types O9–B3, with the majority of the population concentrated in the B1–B2 types. Across all four confirmed populations, the effective temperatures span 17.29–42.45 kK, with a median of 24.76 kK. While the spectral classifications directly support an O9–B3 range, the temperature distribution suggests that the population may extend to earlier spectral types, potentially reaching O5. Across all four populations, the $\log g$ values span 2.47–4.60, with a median of 3.88. Twenty stars have ESP-HS surface gravities below $\log g = 3.2$ (Table 5), suggesting that they may have evolved beyond the main sequence. However, spectroscopic follow-up is required to verify their surface gravities and evolutionary states.

On the HR diagram (Figure 5), most β Cep stars are located within the mass range of 7–15 $M_\odot$, with only a few objects at lower or higher masses. Most stars located outside the lower boundary of the region of overlapping p- and g-mode instability, as well as within the region where only g modes are expected to be unstable, are Hybrid pulsators or Hybrids in EB systems. However, these regions are not exclusively occupied by Hybrid pulsators, and a few "pure" β Cep pulsators also lie outside the displayed instability regions. The extended sample shows the same overall temperature–luminosity distribution, while presenting additional lower luminosity stars and a broader luminosity distribution. This broader spread is expected because these luminosities are derived from a single Gaia band rather than from the weighted three-band Bayestar calculation.

This catalog represents the largest compilation of β Cep stars, allowing us to study them statistically as a group. Additionally, this collection of reliably classified β Cep pulsators can be used for selecting targets for follow-up observations for complete asteroseismic studies, such as the GAP project (Shitrit & Arcavi 2024), and for ensemble studies such as those of Fritzewski et al. (2025a) and Vanrespaille et al. (2026). We hope that this catalog thus provides an essential contribution to advancing our understanding of the interiors and evolution of massive stars.

This research was supported in part by the Polish National Center for Science (NCN) through grants 2015/18/A/ST9/00578 and 2021/43/B/ST9/02972. We are grateful to Joshua Pepper for his work on the KELT data in the archival data search part of this work.

Software: astropy (Astropy Collaboration et al. 2013, 2018, 2022), Lightkurve (Lightkurve Collaboration et al. 2018), dustmap (Green 2018), SciPy (Virtanen et al. 2020), scikit-learn (Pedregosa et al. 2011), STAR SHADOW (IJspeert et al. 2024)

APPENDIX

A. LITERATURE REVIEW SOURCES

In Table A1 we present the sources from which the literature-review β Cep stars were collected (Section 2.1).

Table A1. Summary of the literature-review sources.

Source	Total Number of Candidates	Missing TESS Light Curve
SIMBAD; Wenger et al. (2000)	7	2
VSX; Watson et al. (2022)	1401	27
Hill (1967)	1	0
Pigulski et al. (1997)	1	0
Samus' et al. (2003)	1	0
Bouzid & Sterken (2004)	2	0
Handler (2005)	5	0
Stankov & Handler (2005)	191	11
De Cat et al. (2006)	1	0

Table A1 *continued*

Table A1 *(continued)*

Source	Total Number of Candidates	Missing TESS Light Curve
Narwid et al. (2006)	1	1
Pietrukowicz et al. (2006)	1	0
Pigulski & Michalska (2007)	2	0
Pigulski & Pojmański (2007)	4	0
Telting et al. (2007)	100	4
Majewska-Świerzbinowicz et al. (2008)	6	0
Pigulski & Pojmański (2008a)	120	0
Pigulski & Pojmański (2008b)	1	0
Walker (2008)	1	0
Antoci et al. (2009)	1	0
Degroote et al. (2009)	1	0
Hubrig et al. (2009)	2	0
Jurcsik et al. (2009)	1	0
Michalska et al. (2009)	1	0
Balona et al. (2011)	5	0
Handler & Meingast (2011)	6	0
Hu et al. (2011)	1	0
Lehmann et al. (2011)	2	0
Neiner & Floquet (2011)	1	0
Paparó et al. (2011)	1	0
Uytterhoeven et al. (2011)	1	0
McNamara et al. (2012)	2	2
Zhang et al. (2012)	1	0
Drobek et al. (2013)	2	0
Meingast et al. (2013)	3	0
Pápics et al. (2013)	2	0
Pietrukowicz et al. (2013)	48	47
Sarro et al. (2013)	15	5
Ulusoy et al. (2013)	1	0
Bakış et al. (2014)	1	0
Díaz-Fraile et al. (2014)	3	0
Lata et al. (2014)	3	0
Saesen et al. (2014)	6	0
Balona et al. (2015)	6	1
Bass & Borne (2016)	1	0
Lata et al. (2016)	1	0
Laur et al. (2017)	11	1
Samus' et al. (2017)	2	0
Skarka et al. (2017)	1	1
Bognár et al. (2018)	1	0
Burssens et al. (2019)	2	0

Table A1 *continued*

Table A1 *(continued)*

Source	Total Number of Candidates	Missing TESS Light Curve
Lata et al. (2019)	1	0
Moździerski et al. (2019)	4	0
Xue et al. (2019)	5	0
Balona & Ozuyar (2020)	4	0
Labadie-Bartz et al. (2020)	52	0
Southworth et al. (2020)	1	0
Kołaczek-Szymański et al. (2021)	2	0
Lee & Hong (2021)	1	0
Stassun et al. (2021)	1	0
Zhuo et al. (2021)	2	0
Bowman et al. (2022)	5	0
Southworth & Bowman (2022)	11	0
Chen et al. (2022)	5	0
Burssens et al. (2023)	1	0
Rimoldini et al. (2023)	1450	29
Shi et al. (2023)	14	0
Eze & Handler (2024)	90	0
Hey & Aerts (2024)	165	2
Shi et al. (2024)	99	0
Çakırlı et al. (2025)	2	0
Chakraborty et al. (2025)	16	13
Fritzewski et al. (2025b)	27	1
Kemp et al. (2025)	3	0
Nazé et al. (2025)	4	1
Shi et al. (2025)	77	0
Zummer et al. (2026)	1	0

Note—The numbers include duplicates between different literature sources.

B. LUMINOSITY AND EXTINCTION METHOD COMPARISONS

We compare the luminosity and extinction estimates calculated in Section 3.3 and used in the HR diagrams presented in Section 7.4 to assess how the choice of luminosity method affects both the derived values and the number of stars that can be included in the HR diagrams. We retain confirmed β Cep and Hybrid pulsators, including EB systems, with reliable Bayestar19 estimates (`bayestar_converged`=True and `bayestar_reliable_dist`=True).

For each comparison, we use only the mutual sample, namely stars with finite values for both quantities being compared:

(a) Weighted three-band versus G-only Bayestar luminosities, both calculated assuming solar metallicity. This comparison contains 323 stars. The weighted three-band calculation requires reliable Bayestar estimates and Gaia G, BP, and RP photometry.

(b) Weighted three-band Bayestar luminosities versus G-only luminosities calculated using the ESP-HS A_G values, assuming solar metallicity. This comparison contains 323 stars.

(c) Bayestar versus ESP-HS A_G estimates. This comparison contains 323 stars.

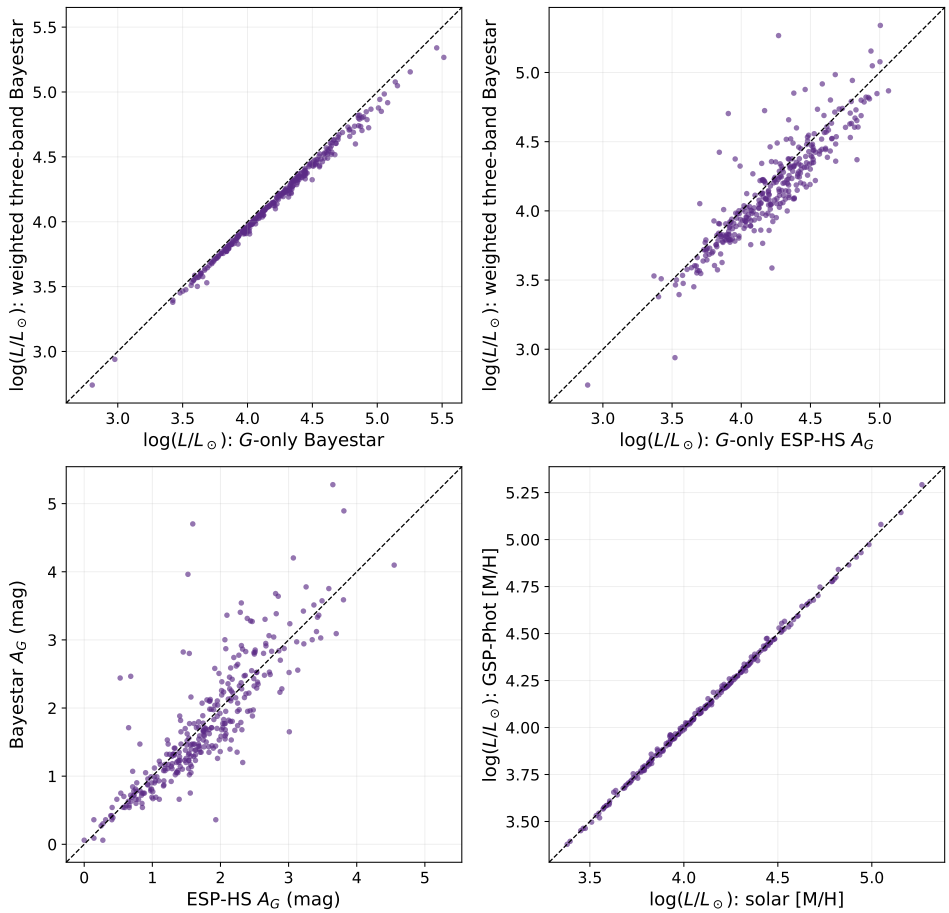

Figure B1. Comparison of the luminosity and extinction estimates used for the HR diagrams. The panels, read from upper left to lower right, show comparisons (a)–(d), respectively: weighted three-band versus G-only Bayestar luminosities assuming solar metallicity; weighted three-band Bayestar versus G-only ESP-HS-A_G luminosities assuming solar metallicity; Bayestar versus ESP-HS A_G estimates; and weighted three-band Bayestar luminosities calculated using solar and GSP-Phot metallicities. The dashed lines indicate equality.

(d) Weighted three-band Bayestar luminosities calculated using solar and GSP-Phot metallicities. This comparison contains 245 stars because it additionally requires an available GSP-Phot metallicity.

Figure B1 shows these four comparisons. In (a), the weighted three-band luminosities are lower than the G-only Bayestar luminosities by a median of 0.048 dex. In (b), the median difference is -0.081 dex and the scatter is larger. In (c), Bayestar gives lower extinction values than ESP-HS by a median of 0.077 mag. Finally, (d) shows a median difference of only -0.004 dex, indicating that the solar-metallicity assumption has a negligible effect on the paired luminosities.

Together with the corresponding sample sizes, these comparisons motivate the two HRD luminosity choices. We retain the weighted three-band Bayestar luminosity as the primary estimate for the left panel of Figure 5 because it uses all three Gaia bands and reliable Bayestar19 extinction estimates. Although the corresponding G-only Bayestar luminosities agree closely with the weighted three-band Bayestar luminosities, they show a small systematic offset and provide the same 323 stars under the Bayestar-quality selection. Thus, the G-only Bayestar method does not extend the HRD sample. We retain the G-only ESP-HS-A_G luminosity for the extended HRD sample in the right panel of Figure 5 because it is available for substantially more stars; it provides 783 stars, including all 323 stars in the Bayestar sample and 460 additional stars. Its broader scatter relative to the weighted three-band values supports treating it as a separate estimate and including the empirical dispersion as an additional uncertainty. The difference between the Bayestar and ESP-HS extinction estimates further supports retaining the two methods separately rather than combining them. Finally, because the solar- and GSP-Phot-metallicity luminosities agree almost exactly for the

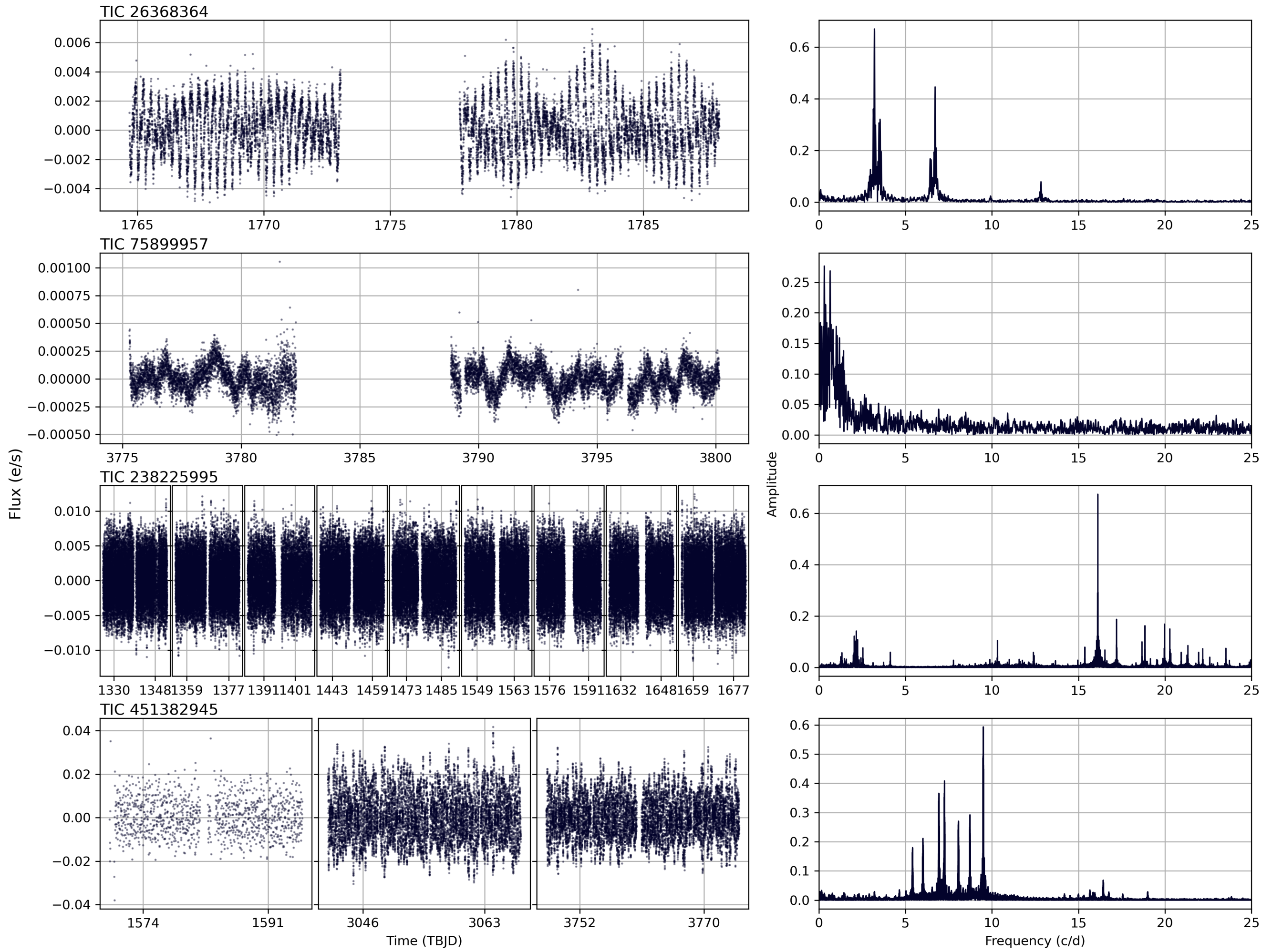

Figure D2. Examples of the four types of impostors described in Section 5. All the stars in this plot were mentioned as confirmed or candidate β Cep stars. The left panels show the TESS light curves and the right panels show their Lomb-Scargle periodograms. The first panel (from the top) is for a β Cep candidate that was found to be an SPB star with rotation that shifts the "real" SPB pulsation frequency to higher frequencies through harmonics. The second panel is for a GDOR star, the third displays a light curve showing GDOR + DSCT pulsations, and the fourth is for a star displaying DSCT pulsations.

stars with both estimates, we adopt solar metallicity for the HRD luminosities, which also permits the inclusion of more stars without GSP-Phot metallicities.

C. STELLAR PARAMETERS FROM SPECTRA

In Table C2 we present the spectral observation log and the stellar parameters resulting from the analysis of the spectra (see Section 4), namely T_{eff}, $\log g$ and $v \sin(i)$. We also present the classification of each star as classified in this work. Stars with no classification in the table do not have TESS light curves and therefore were not reclassified in this work. Note that some of the stars for which we collect spectra were reclassified in this work as non-β Cep pulsators, but we still publish their spectroscopic results here for future use.

D. VISUAL CLASSIFICATION

Figure D2 shows examples of possible β Cep impostor types encountered during the classification process described in Section 5. In Figure D3 we present a screenshot of the GUI used for the visual classification described in Section 5.

Table C2. Spectral observation log and stellar parameters computed from the spectra. The letters: H, M and L under the "Mode" column stands for the high, medium and low resolution, respectively. The reference numbers in the table indicate the studies from which the spectral classifications were adopted. The "Classification" column refers to the classification assigned to the star in this work.

Name	Spec. Type	Obs. Date	Num.	SNR	Mode	T_{eff} (K)	$\log g$	$v \sin i$ (km/s)	Ref.	Classification
BW Cru	B2 III	Jan., Apr. 2018	2	208, 230	H	$22{,}000 \pm 1000$	3.50 ± 0.15	94 ± 5	1	Hybrid
HN Aqr	B2	June 2019, Jul, Aug 2022	4	55, 130, 85, 90	M, L	$22{,}000 \pm 1000$	3.80 ± 0.10	36 ± 3	2	BCEP
KZ Mus	B2 III	Feb. 2018	1	130	H	$20{,}000 \pm 1000$	3.75 ± 0.10	44 ± 3	3	BCEP
V4386 Sgr	B1 II	Apr. 2018	2	170,215	H	$27{,}000 \pm 1000$	3.90 ± 0.15	309 ± 17	4	BCEP, EB
V916 Cen	B0.5IVne	Feb., May 2019	2	275, 150	M	$25{,}000 \pm 1000$	3.80 ± 0.10	84 ± 4	5	BCEP, EB
BD -02 4752	B0.5 V	Apr., May 2019	2	35, 50	M	$25{,}000 \pm 1000$	4.25 ± 0.15	95 ± 5	6	BCEP
CD -31 17605		Aug. 2022	2	100, 65	L	$23{,}000 \pm 1000$	4.00 ± 0.10	38 ± 2	7	Hybrid
CD -38 4128	B1 V	May 2019	1	140	M	$21{,}000 \pm 1000$	3.70 ± 0.15	31 ± 2	8	BCEP, EB
CD -44 4596	B1 III	Feb. 2019	1	150	M	$23{,}000 \pm 1000$	4.00 ± 0.10	48 ± 2	9	Hybrid, EB
CD -49 3738		Dec. 2018	1	100	M	$23{,}000 \pm 1000$	3.75 ± 0.10	107 ± 2		Hybrid
HD 18100	B5 II/III	Nov. 2018	1	140	H	$27{,}000 \pm 1000$	4.00 ± 0.15	228 ± 6	10	Hybrid
HD 46149	O8.5 V	Jan. 2018	2	75, 110	H	$29{,}000 \pm 1500$	4.00 ± 0.15	97 ± 3	11	
HD 46994	B2/3V	Sep., Oct. 2019	2	180, 220	H	$21{,}000 \pm 1000$	4.00 ± 0.10	285 ± 8	12	SPB
HD 48553	B2 III	Dec. 2017	1	178	H	$21{,}000 \pm 1000$	3.80 ± 0.20	14 ± 2	13	Hybrid
HD 59864	B1/2Ib/II	Oct. 2018	2	165, 220	H	$26{,}000 \pm 1000$	3.75 ± 0.10	18 ± 1	10	Hybrid
HD 61193	B2 V	Apr. 2018	1	250	H	$23{,}000 \pm 1000$	4.25 ± 0.10	221 ± 6	14	Hybrid
HD 71913	B1/2 II	Dec. 2018, Feb. 2019	2	230, 170	H	$20{,}000 \pm 500$	3.25 ± 0.20	42 ± 2	10	BCEP
HD 73568	B2 III/IV	Jan. 2018	1	100	H	$22{,}000 \pm 1000$	3.50 ± 0.10	86 ± 4	14	Hybrid
HD 73918	B5 III	May 2019	1	220	M	$14{,}000 \pm 200$	3.70 ± 0.10	121 ± 3	10	Non-BCEP
HD 74339	B2/3II/III	Feb. 2019	1	180	M	$21{,}000 \pm 1000$	3.50 ± 0.10	48 ± 2	14	Hybrid
HD 75290	B3/5 V	Dec. 2017	1	150	H	$15{,}000 \pm 1000$	4.50 ± 0.10	297 ± 8	14	SPB
HD 86248	B2 II	Jan., June 2019	2	80,95	M	$22{,}000 \pm 500$	3.70 ± 0.10	41 ± 1	10	BCEP
HD 87592	B1 IV	Dec. 2017	2	170,140	H	$25{,}000 \pm 1000$	3.75 ± 0.15	18 ± 2	3	Hybrid
HD 90288	B2 III/IV	Jan. 2018	1	130	H	$25{,}000 \pm 1000$	4.25 ± 0.10	143 ± 5	3	Hybrid
HD 92291	B1 Ib/II	Feb. 2018	1	150	H	$23{,}000 \pm 1000$	3.60 ± 0.10	31 ± 3	3	BCEP
HD 94065	B0/1 III/IV	Feb. 2018	1	180	H	$23{,}000 \pm 1000$	3.50 ± 0.10	37 ± 3	3	Hybrid
HD 94345	B0/1 IV	Jan., Apr. 2018	2	100,170	H	$22{,}000 \pm 1000$	3.25 ± 0.10	42 ± 3	3	Hybrid
HD 96882	B1 II/III	June 2019	1	160	H	$24{,}000 \pm 1000$	3.75 ± 0.10	92 ± 3	3	Hybrid
HD 96901	B1 III/IV	Feb. 2018	1	160	H	$24{,}000 \pm 500$	3.75 ± 0.10	75 ± 3	3	Hybrid
HD 96927	B3 III	Jan., June 2019	2	140,150	H	$23{,}000 \pm 500$	3.70 ± 0.10	63 ± 2	14	BCEP
HD 101838	B0.5/1 III	Jan., May 2019	2	100,210	M	$23{,}000 \pm 1000$	3.30 ± 0.15	183 ± 2	3	BCEP, EB
HD 102505	B1 IV	Apr. 2018	2	160,160	H	$26{,}000 \pm 1000$	3.75 ± 0.10	91 ± 4	3	Hybrid
HD 106345	B2 III	Apr. 2019	1	150	H	$22{,}000 \pm 500$	3.75 ± 0.10	21 ± 1	3	Hybrid
HD 112481	B2 II/III	Feb., July 2019	2	80,175	H	$24{,}000 \pm 500$	3.50 ± 0.10	42 ± 1	14	Hybrid
HD 119910	B2 III/IV	June, July 2019	2	170,200	H	$21{,}000 \pm 500$	3.75 ± 0.10	18 ± 2	3	Hybrid
HD 126357	B1 III	Feb. 2018	1	160	H	$25{,}000 \pm 1000$	3.75 ± 0.10	71 ± 3	3	Hybrid
HD 129929	B2	Feb., June 2019	2	90,140	H	$25{,}000 \pm 1000$	3.90 ± 0.10	19 ± 1	10	Hybrid
HD 131805	B5 V	June, July 2019	2	60,120	H	$17{,}000 \pm 1000$	4.00 ± 0.20	270 ± 7	3	SPB
HD 140543	B1 Iab/b	Mar., June 2019	2	130,150	H	$28{,}000 \pm 1000$	3.30 ± 0.20	324 ± 10	12	Hybrid
HD 145794	B2 II/III	Apr. 2018	1	250	H	$17{,}000 \pm 1000$	3.50 ± 0.10	148 ± 5	14	BCEP
HD 146442	B2 III	May, June 2019	2	120,130	M	$22{,}000 \pm 500$	3.70 ± 0.10	44 ± 1	14	BCEP
HD 147985	B1/2 II/III	Feb., Apr. 2019	2	110,190	H	$22{,}000 \pm 1000$	4.00 ± 0.10	126 ± 4	14	Hybrid
HD 149100	B2 III	May 2018	1	210	H	$17{,}000 \pm 1000$	3.90 ± 0.10	127 ± 5	14	Hybrid
HD 151158	B2 Ib/II	Sep. 2019	1	175	H	$6{,}900 \pm 100$	4.00 ± 0.10	49 ± 2	14	Non-BCEP
HD 151654	F0 V	Apr. 2018	1	210	H	$13{,}000 \pm 1000$	4.20 ± 0.10	46 ± 3	13	
HD 152162	B2 III	Mar., July 2019	2	125,150	H	$21{,}000 \pm 500$	3.75 ± 0.10	18 ± 2	14	Hybrid
HD 152372	B2 III/IV	Mar., June 2019	2	130,150	H	$23{,}000 \pm 500$	3.90 ± 0.10	19 ± 1	14	Hybrid
HD 153772	B2 V	June, July 2019	2	90,190	H	$21{,}000 \pm 1000$	4.10 ± 0.10	72 ± 1	14	BCEP
HD 156172	O9 V	July, Sep. 2019	2	110,180	H	$33{,}000 \pm 1500$	4.00 ± 0.10	270 ± 10	4	BCEP
HD 156321	B2 V	Sep. 2019	2	20,100	H	$25{,}000 \pm 500$	4.00 ± 0.10	123 ± 3	6	Hybrid
HD 156662	B2 III	Feb. 2018	1	165	H	$22{,}000 \pm 1000$	3.50 ± 0.10	109 ± 4	14	BCEP
HD 160233	B1 II	Apr. 2018	1	130	H	$24{,}000 \pm 1000$	3.90 ± 0.10	135 ± 5	13	
HD 166540	B1 Ib	Apr. 2018	2	90	H	$29{,}000 \pm 1000$	3.90 ± 0.15	35 ± 3	12	Hybrid
HD 167451	B1 Ib	Mar., May 2019	2	120,120	H	$28{,}000 \pm 1500$	3.25 ± 0.15	69 ± 2	12	BCEP
HD 167743	B2 Ib	Apr., June 2019	2	100,140	M	$23{,}000 \pm 1000$	3.75 ± 0.10	58 ± 1	12	BCEP
HD 168050	B3/5 Ib	Mar., April 2019	2	40,80	M	$23{,}000 \pm 1500$	4.00 ± 0.20	62 ± 3	12	BCEP, EB
HD 171305	B2 II	June, Aug. 2019	2	90,100	H	$21{,}000 \pm 500$	3.50 ± 0.10	16 ± 1	13	BCEP
HD 178987	B2 II	Mar., Apr. 2019	2	100,140	M	$21{,}000 \pm 1000$	3.50 ± 0.10	135 ± 2	14	BCEP
HD 186610	B2 Ib/II	Mar., May 2019	2	80,130	M	$20{,}000 \pm 500$	3.25 ± 0.10	37 ± 1	13	BCEP
HD 187536	B3 II	Aug. 2022	3	110, 85, 155	L	$24{,}000 \pm 1000$	3.50 ± 0.10	173 ± 4	10	Hybrid
HD 357657	B	July, Aug. 2022	2	90, 105	L	$24{,}000 \pm 1000$	4.0 ± 0.10	38 ± 2	6	Hybrid

Note— Spectral type references: (1) Schild (1970); (2) Reed (2003); (3) Houk & Cowley (1975); (4) Garrison et al. (1977); (5) Fitzgerald & Miller (1983); (6) Wenger et al. (2000); (7) O'Donoghue et al. (2013); (8) Herbst (1975); (9) Münch (1952); (10) Houk (1982); (11) Sota et al. (2011); (12) Houk & Smith-Moore (1988); (13) Houk & Swift (1999); (14) Houk (1978).

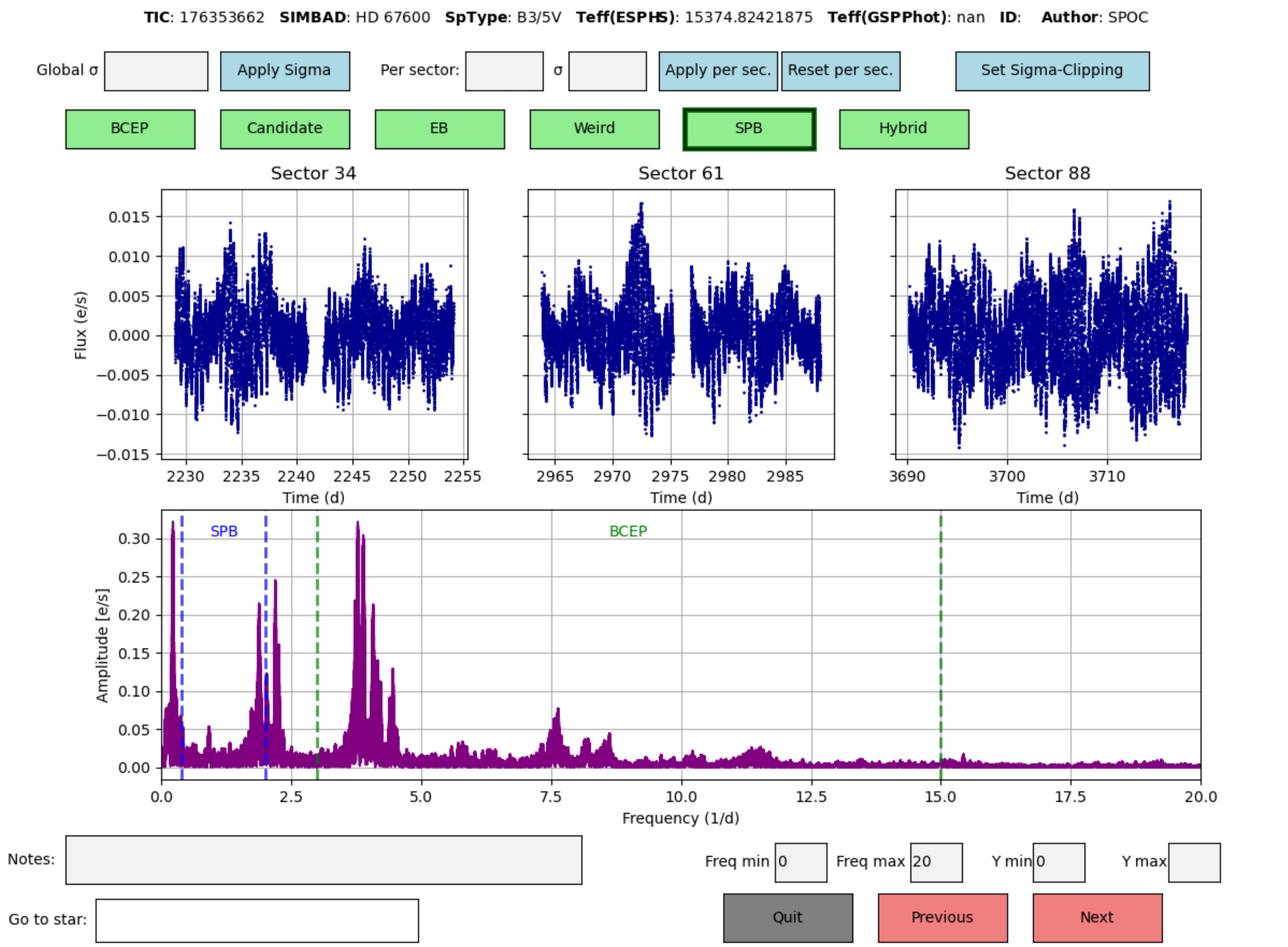

Figure D3. A screenshot of the visual-classification GUI developed for this work. The top annotations display the stellar metadata (TIC, SIMBAD ID, spectral type, effective temperature from ESP-HS and GSP-Phot pipelines and the TESS pipeline from which the light curve is obtained). Below these annotations are the sigma-clipping controls, which allow either global sigma clipping of the full light curve or sector-specific clipping, with the option to save the processed data. Below these controls are the classification buttons. The top panel of plots shows the TESS light curve, divided into sector-by-sector subplots. The bottom panel displays the Lomb–Scargle periodogram together with the β Cep and SPB pulsation frequency ranges. At the bottom of the interface, a text box is provided for notes, along with controls for adjusting the x- and y-axis limits, and for loading a specific star.

E. DESCRIPTION OF THE CATALOG

The machine-readable catalog is provided electronically (**a link will be added**). Table E4 presents the first nine columns and first 45 rows of the catalog, and Table E3 describes its columns. It contains one adopted row per star. When both SPOC and QLP light curves are available, we retain QLP if QLP_OVER_SPOC=1 and otherwise retain SPOC. Empty entries indicate unavailable data or derived parameters.

F. EFFECT OF CADENCE EQUALIZATION (BINNING) ON PULSATION-PARAMETER EXTRACTION

We investigate the impact of binning on the recovery of pulsation parameters in TESS light curves, focusing on the frequencies and amplitudes derived from iterative prewhitening using STAR SHADOW (see Section 3.2).

The strength of the impact depends on the ratio between the oscillation period P and the bin width Δt. For modes with $P \gg \Delta t$ (equivalently $f \ll 1/\Delta t$), as is the case for the β Cep pulsations analyzed here, the signal varies little within each bin, and the measured pulsation properties are not expected to be significantly affected. In contrast, for

Table E3. Description of the columns in the machine-readable catalog.

Columns	Description
target_id, TIC, TIC_sep, source_id, Gaia_sep, designation, ra, dec, RA_Simbad, Dec_Simbad, TIC_MULT_MATCH, Gaia_MULT_MATCH, number_of_gaia_candidates, solution_id	Identifiers, coordinates, cross-match separations (arcsec), multiple-match flags, number of Gaia candidates, and Gaia DR3 solution identifier.
Classification, SpType_SIMBAD, Vmag_SIMBAD, vsini_SIMBAD, SigmaClipping_classification, SigmaValue_classification, Notes_classification, cluster?	Final classification; SIMBAD spectral type, V magnitude, and $v \sin i$; visual-classification clipping information and notes; and cluster-membership flag. SigmaClipping_classification indicates whether sigma clipping was applied, and SigmaValue_classification gives either the global clipping value or sector-specific values in the form S<sector>=<value>.
Classification_history_literature, SIMBAD_Classification, Notes, Ref., Year, Link, Year_earliest, Year_history, Ref_earliest, Ref_history	Literature classifications, references, publication years, links, and notes.
TESS_lc, TESS_pipeline, TESS_sectors, TESS_exp_time, QLP_OVER_SPOC	TESS_lc indicates whether a TESS light curve is available (1) or unavailable (0); adopted pipeline, analyzed sectors, exposure time (s), and flag indicating that QLP was adopted over SPOC.
ROT, ELL, EB, HEARTBEAT, ONLY_SLF, SLF, DSCT, GDOR, CONST, QLP_BAD, SAT, SPEC_WRONG, BLEND, NEARBY_STAR, LOW_FREQ_HARMONICS, MANY_FREQS, HIGH_FREQS, COMB	Visual-classification and data-quality flags defined in Section 5. A value of 1 denotes a secure identification and 0.5 a tentative identification.
parallax, parallax_error, parallax_over_error, pm, pmra, pmdec, ruwe, phot_*_mean_mag, phot_*_mean_flux_over_error, bp_rp, bp_g, g_rp, radial_velocity, radial_velocity_error	Gaia DR3 astrometric, photometric, color, and radial-velocity parameters used in this work. Here phot_*_mean_mag and phot_*_mean_flux_over_error refer to the G, BP, and RP bands.
teff_gspphot, logg_gspphot, mh_gspphot, and associated _lower and _upper columns; teff_esphs, logg_esphs, ag_esphs, ebpminrp_esphs, and associated _uncertainty columns	Gaia DR3 GSP-Phot and ESP-HS atmospheric parameters, reported bounds, and uncertainties.
bayestar_converged, bayestar_reliable_dist, A_G_bayestar, M_G_bayestar, M_G_bayestar_err, M_BP_bayestar, M_RP_bayestar, M_G_esphs, M_G_esphs_err, log_L_divide_Lsun_*	Bayestar19 flags and extinction, extinction-corrected absolute magnitudes, and luminosities used for the HR diagrams and luminosity-method comparisons. The _solar luminosities use solar-metallicity bolometric corrections; the corresponding unsuffixed weighted-mean luminosities use the Gaia GSP-Phot metallicity.
p_orb_*, depth_*_measured, depth_*_final_model, t_*_measured, t_*_final_model, e, w, i, r_sum, r_rat, sb_rat, ratio1_1--ratio4_3, EB_cand_flag, EB_flag, ROTMOD_flag, EB_score	STAR SHADOW orbital, eclipse, EB-model, and EB/rotational-modulation parameters. See Section 3.2 for the analysis procedure
f1--f30, a1--a30, ph1--ph30, f1_final--f30_final, a1_final--a30_final, ph1_final--ph30_final	First and final STAR SHADOW frequency, amplitude, and phase sets.

Table E4. Excerpt of the machine-readable catalog. The first 45 rows and first 9 columns are shown; the complete table is available electronically.

target_id	TIC	TIC_sep	source_id	Gaia_sep	designation	ra	dec	Classification
HD 217035	13212836.0	0.0297427741602749	2207297149288415232	0.1928143579219829	Gaia DR3 2207297149288415232	344.1289404042378	62.868366731474325	Weird
TIC 329992262	329992262.0	0.0795664420220739	2198645573310089600	0.079566442025338	Gaia DR3 2198645573310089600	333.14160464395064	57.25803726746035	BCEP
* 23 Tau	61139113.0	0.8336416088740166	65205373152172032	0.8023603560181609	Gaia DR3 65205373152172032	56.58167144917715	23.94814381017594	SPB
NGC 6231 239	339567650.0	0.1986717937769871	5966508992127646464	0.1976138585929844	Gaia DR3 5966508992127646464	253.5650733309733	-41.86926956956006	Weird
V* V1205 Sco	339567743.0	0.0361442906564723	5966508987825250048	0.036911038270429	Gaia DR3 5966508987825250048	253.56556984806772	-41.86108233261907	Weird
* gam Peg	51942308.0	0.1466761237982191	2769202742740232960	0.1715451775218926	Gaia DR3 2769202742740232960	3.3089703843753013	15.183550741446307	Hybrid
V* V909 Cas	390122587.0	0.0256695636960721	510001703986507520	0.0259140491112362	Gaia DR3 510001703986507520	24.160629451723917	61.43163626126622	BCEP
V* V1155 Cas	399436828.0	0.0167669529918569	511217592043001216	0.0181879021990801	Gaia DR3 511217592043001216	26.662482725248275	61.23501371190087	BCEP
BD+56 501	264613043.0	0.0266511533340822	458372795471717888	0.0232339562085865	Gaia DR3 458372795471717888	34.62430147708934	57.15087308127002	Hybrid
BD+56 508	264731122.0	0.0251906605466908	458379701779206400	0.0221381372097867	Gaia DR3 458379701779206400	34.70007084831595	57.28551863787359	BCEP
BD+56 520	264730502.0	0.0128627568456106	458377743274230784	0.0180362613550536	Gaia DR3 458377743274230784	34.750863931250336	57.14563958733677	. . .
V* V619 Per	348607672.0	0.0210737028890237	458454606008606336	0.0206041998312068	Gaia DR3 458454606008606336	35.51159515649917	57.14027850945556	BCEP
V* V595 Per	348607604.0	0.0241940445549815	458407670603899648	0.0282639679739983	Gaia DR3 458407670603899648	35.53570352714599	57.12454836175567	Weird
* del Cet	328161938.0	0.1957591157512272	2498783458525988992	0.2142599834166615	Gaia DR3 2498783458525988992	39.87071163754866	0.3284966543857036	Hybrid
V* KP Per	65166720.0	0.0981306767959816	241678947918118912	0.0972575391803758	Gaia DR3 241678947918118912	53.16241159653567	44.85573265544764	BCEP
* eps Per	187107884.0	0.4364421852004821	229898024422755840	0.463694421894351	Gaia DR3 229898024422755840	59.463595170524904	40.0100950978535	BCEP
* nu. Eri	229087301.0	0.0888652771431315	3204884534485995264	0.0766973876220919	Gaia DR3 3204884534485995264	69.07976184342182	-3.3524812188642006	Hybrid
TIC 4254645	4254645.0	0.0508950229249243	3214077516844988800	0.0508950229256123	Gaia DR3 3214077516844988800	81.11923705133687	-2.3971524975189644	EB
* psi02 Ori	264540478.0	0.0226811299659237	3235897703054775936	0.0233310322647902	Gaia DR3 3235897703054775936	81.70929343540975	3.0956682931066135	EB
* bet CMa	34590771.0	0.0646075947169533	. . .	. . .	. . .	. . .	. . .	BCEP
* ksi01 CMa	47763235.0	0.0976425604404019	2924859847973986048	0.1107977994277122	Gaia DR3 2924859847973986048	97.9640099410608	-23.418394841586725	BCEP
* 15 CMa	78897024.0	0.1519963835896338	2932263546963330176	0.1180243757102372	Gaia DR3 2932263546963330176	103.38708452690732	-20.224232345171853	BCEP
* 19 Mon	269087549.0	0.0722039668161381	3101768554465447936	0.0728462047908323	Gaia DR3 3101768554465447936	105.72822063907358	-4.239222040833818	Hybrid
* 27 CMa	65803653.0	0.1073101367779548	5610288149803056896	0.131030112807695	Gaia DR3 5610288149803056896	108.5633486897137	-26.35248705694927	Hybrid
V* V350 Pup	112923257.0	0.0969961120344361	5591456230038742016	0.0947352858055188	Gaia DR3 5591456230038742016	112.64195532159609	-34.09057544918967	Hybrid
V* PT Pup	349043273.0	0.1278088094289274	5716409335624704768	0.1190990386233505	Gaia DR3 5716409335624704768	114.17094973342256	-19.702323468770643	BCEP
V* QU Pup	143488434.0	0.1538874939286954	5532548142233447424	0.158404749691211	Gaia DR3 5532548142233447424	117.91812003760556	-42.88816971673171	BCEP
V* V372 Car	340985103.0	0.1564823229392656	5488339734612857984	0.1555052155381935	Gaia DR3 5488339734612857984	118.12388808016225	-54.367125332398615	Hybrid
HD 71913	56630835.0	0.1058910789731094	5543515083529532928	0.1043260320653663	Gaia DR3 5543515083529532928	127.17916162880256	-34.73159605638968	BCEP
V* KK Vel	31921921.0	0.141989633579199	5330841772046764928	0.1382864181840643	Gaia DR3 5330841772046764928	136.92711698409929	-44.63242192642359	Hybrid
V* IL Vel	293680998.0	0.0850549785229819	5311655328520521600	0.0843976176997563	Gaia DR3 5311655328520521600	139.37976450535623	-52.83873184173844	BCEP
HD 90288	464296873.0	0.1466273724611769	5351762420316030464	0.1503278132543991	Gaia DR3 5351762420316030464	155.9870673697272	-57.46454346979854	Hybrid
V* V400 Car	457975914.0	0.1331817719555949	5351451567771333888	0.1315068373452932	Gaia DR3 5351451567771333888	158.70278662979692	-58.150312241218096	BCEP
V* V401 Car	457975502.0	0.1346907660212208	5351448127473759872	0.1340768397027906	Gaia DR3 5351448127473759872	158.87515622648337	-58.20225711685458	BCEP
V* V403 Car	458076392.0	0.1318354701154205	5351448784632614656	0.1328591180272502	Gaia DR3 5351448784632614656	158.91953343554542	-58.21228556917196	BCEP
CD-57 3347	458076501.0	0.1342071368788862	5351447238444368768	0.135016779321505	Gaia DR3 5351447238444368768	158.93034567477468	-58.22599652116463	BCEP
MCW 1182	458076594.0	0.1331674702439058	5351447234127452672	0.133338364404774	Gaia DR3 5351447234127452672	158.95098085669855	-58.23792338618754	BCEP
V* V405 Car	458076374.0	0.1332548972972942	5351448750272913664	0.1339167444294793	Gaia DR3 5351448750272913664	158.95082755114157	-58.20920818265427	BCEP
CPD-57 3517	458076652.0	0.1323882927379847	5351447032285937664	0.1339501522646328	Gaia DR3 5351447032285937664	158.97343952899308	-58.24660999240357	BCEP
V* V440 Car	458076425.0	0.1370882697304282	5351448544114492672	0.1345569093731577	Gaia DR3 5351448544114492672	158.97875274657133	-58.21641354253266	. . .
V* V406 Car	458076353.0	0.1344753120534328	5351448647193741440	0.1354210456896976	Gaia DR3 5351448647193741440	158.99081222124084	-58.2059036528582	Hybrid
HD 92007	458076693.0	0.131191910934169	5351448441035539328	0.1336269101352186	Gaia DR3 5351448441035539328	159.0065737483128	-58.25264812418845	Hybrid
TIC 458076434	458076434.0	0.1280109370613358	5350697989986480896	0.1280109370670217	Gaia DR3 5350697989986480896	159.03466004877737	-58.21786200091148	BCEP, EB
V* KZ Mus	327656776.0	0.1099289858190243	5842913572934429696	0.1101050132517212	Gaia DR3 5842913572934429696	189.82975577557767	-71.62179009925686	BCEP
* bet Cru	405567821.0	0.170459322129786	. . .	. . .	. . .	. . .	. . .	BCEP

Note—A portion is shown here for guidance regarding its form and content.

Table F5. Number of stars from each variability class in the complete sample and in Subsample *I*.

Classification	Complete sample	Subsample I
BCEP	390	341
Hybrid	536	418
BCEP, EB	76	22
Hybrid, EB	12	6

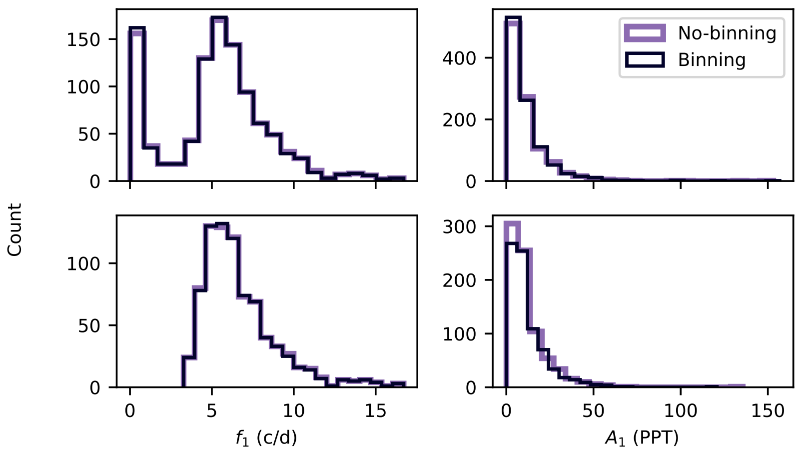

Figure F4. Histograms of the dominant frequency (f_1) and its corresponding amplitude (A_1) for binned and unbinned light curves. The distributions are shown for the complete sample in the top panels and for Subsample I in the bottom panels. While the frequencies remain consistent between the binned and unbinned data, differences in derived amplitudes are more apparent.

modes with $P \sim \Delta t$ or $P < \Delta t$ (i.e. $f \gtrsim 1/\Delta t$), the signal changes significantly across the bin, and a larger effect is expected, particularly the attenuation of measured amplitudes caused by temporal averaging (Murphy 2012).

Murphy (2012) examines cadence effects in Kepler short- and long-cadence data for individual targets, whereas we quantify the effects of cadence equalization across 1,014 TESS targets from our sample, using the same frequency-extraction procedure for the binned and unbinned data. For each star, we compare the dominant frequency and its corresponding amplitude derived from the binned light curve with those derived from the original, unbinned data.

The numbers of stars per class for the complete sample and for Subsample I are displayed in Table F5.

Figure F4 presents the results for the complete sample of 1,014 stars and Subsample I, which includes 787 stars. We find that the frequencies are very stable. Only three stars in the complete sample ($\sim 0.3\%$) and one star in Subsample I ($\sim 0.1\%$) have an absolute frequency difference greater than 0.01 c/d between the binned and unbinned data. For a threshold of 0.001 c/d, 81 stars in the complete sample ($\sim 8.0\%$) and 50 stars in Subsample I ($\sim 6.4\%$) exceed the threshold. For a threshold of 0.0001 c/d, the corresponding numbers are 107 ($\sim 10.6\%$) and 63 ($\sim 8.0\%$), respectively. These results show that binning does not introduce significant shifts in the recovered frequencies in this dataset.

The binned and unbinned analyses yield identical amplitudes for 630 of the 1,014 stars in the complete sample (62.1%) and 536 of the 787 stars in Subsample I (68.1%). Among the stars with different amplitudes, the unbinned amplitude is larger for 237 of 384 objects (61.7%) and 175 of 251 objects (69.7%), respectively. The median $A_{\rm bin}/A_{\rm no\,bin}$ ratios are 0.997 and 0.988, indicating that the binned amplitudes are typically only 0.3% and 1.2% lower than the corresponding unbinned values. Although individual ratios span 0.240–20.195 and 0.678–17.568, respectively, individual amplitudes can differ substantially in isolated cases. Overall, the amplitudes agree closely for most stars, while the unbinned amplitudes tend to be slightly larger when differences are present.

The small differences in the recovered frequencies are consistent with the expectation that, when the pulsation periods are substantially longer than the bin width, binning smooths the measured signal without materially altering its recovered periodicity. Our results confirm that the dominant frequencies remain stable under cadence equalization for this TESS sample.

Based on these results, it is difficult to determine which method is more "correct". Because the recovered frequencies remain stable, the choice between the two methods primarily affects the amplitudes. In the unbinned case, sectors with shorter cadence contribute more data points and therefore carry greater statistical weight in the fitting procedure. This can bias the recovered amplitudes toward values characteristic of the high-cadence data. In contrast, the binning procedure equalizes the cadence across sectors, reducing this imbalance, but at the cost of introducing additional amplitude attenuation due to temporal averaging. This interpretation is supported by our finding that, when the recovered amplitudes differ, the unbinned amplitude is larger in most cases.

We therefore do not recommend one method over the other. We do, however, use the unbinned data for the statistical analysis presented in Section 7.2, because they avoid the additional amplitude attenuation introduced by binning and are therefore more likely to preserve the amplitudes present in the original light curves.

G. STELLAR PARAMETERS STATISTICS

Here we present the additional statistical diagnostics and complete range values used to examine the stellar- and pulsation-parameter distributions discussed in Section 7.2. We present a summary of the ranges, medians and highest peak centers for each parameter and classification in Table G6. For the EB populations, we report peak values only when the sample contains at least 40 objects. The unreported BCEP, EB peaks correspond to samples of $N = 3$–22, whereas the Hybrid, EB samples contain $N = 3$–13 objects.

Figure G5 shows the KDEs, which provide a smoothed representation of the distribution shapes and highlight their peaks, asymmetries, and internal structure. KDEs are not shown for $\log(L/L_\odot)$ in the Hybrid, EB class or for Q in the BCEP, EB and Hybrid, EB classes, because these samples contain only four, three, and three objects, respectively. Figure G6 presents the corresponding ECDFs, which allow the BCEP and Hybrid distributions to be compared independently of the histogram binning.

Table G7 lists the complete results of the statistical tests for the BCEP and Hybrid classes. For each parameter and classification, we report the BIC values of the one- and two-component Gaussian-mixture models and their difference, ΔBIC. Positive ΔBIC values favor the two-component model. We also report the KS statistic and the corresponding raw and Benjamini-Hochberg adjusted p-values for the comparison between the BCEP and Hybrid distributions. The KS statistic and its corresponding raw and Benjamini-Hochberg-adjusted p-values are repeated for the two classification rows because each KS test compares the two classes directly. We present the interpretations of these results in Section 7.2.

H. VELOCITY ANALYSIS

Table H8 lists the stars identified as empirical kinematic outliers. We select stars with tangential velocities exceeding three standard deviations above the sample median ($183.509, \mathrm{km}, \mathrm{s}^{-1}$), as well as stars with directional deviations exceeding three standard deviations ($46.303°$) and tangential velocities greater than $20, \mathrm{km}, \mathrm{s}^{-1}$ (see Section 7.6). These criteria identify 16 stars with exceptional tangential velocities and 39 with exceptional directions; two stars satisfy both criteria.

Figure H7 presents kernel density estimates of the proper-motion, tangential-velocity, and space-velocity distributions. These estimates provide a complementary visualization of the distribution shapes and possible bimodality discussed in Section 7.6.

REFERENCES

Aerts, C. 2000, A&A, 361, 245

Aerts, C., Christensen-Dalsgaard, J., & Kurtz, D. W. 2010, Asteroseismology, Astronomy and Astrophysics Library, Springer Berlin Heidelberg

Table G6. Summary of the value ranges, medians and highest peaks for each stellar and pulsation parameter for the different classes and for all populations combined.

Parameter	Class	Range	Median	Peak
Distance (kpc)	BCEP	0.28–9.08	2.39	2.38
	Hybrid	0.15–8.67	2.21	1.91
	BCEP, EB	0.44–6.11	2.06	2.38
	Hybrid, EB	0.65–5.43	2.02	–
	All	0.15–9.08	2.31	2.38
m_V (mag)	BCEP	1.25–13.66	10.26	10.61
	Hybrid	0.58–14.06	9.83	9.62
	BCEP, EB	0.97–12.21	9.59	9.62
	Hybrid, EB	5.99–12.33	10.00	–
	All	0.58–14.06	9.96	9.62
M_G (mag)	BCEP	(−6.76)–1.50	−3.46	−3.17
	Hybrid	(−6.63)–(−0.73)	−3.29	−3.17
	BCEP, EB	(−5.44)–(−2.37)	−3.75	–
	Hybrid, EB	(−5.31)–(−1.74)	−3.10	–
	All	(−6.76)–1.50	−3.37	−3.17
M_{BP} (mag)	BCEP	(−7.50)–1.65	−3.54	−3.26
	Hybrid	(−7.60)–(−0.78)	−3.42	−3.26
	BCEP, EB	(−5.66)–(−2.51)	−3.93	–
	Hybrid, EB	(−5.64)–(−1.73)	−3.20	–
	All	(−7.60)–1.65	−3.49	−3.26
M_{RP} (mag)	BCEP	(−5.31)–1.25	−3.11	−3.00
	Hybrid	(−4.92)–(−0.55)	−3.05	−3.00
	BCEP, EB	(−4.89)–(−2.14)	−3.44	–
	Hybrid, EB	(−4.62)–(−1.78)	−2.95	–
	All	(−5.31)–1.25	−3.11	−3.00
$T_{\rm eff}$ (kK)	BCEP	18.91–42.45	25.29	24.41
	Hybrid	17.29–36.26	24.44	23.58, 24.41
	BCEP, EB	17.37–40.00	24.74	25.25
	Hybrid, EB	21.84–34.97	23.09	–
	All	17.29–42.45	24.76	24.41
$\log g$	BCEP	3.11–4.49	3.89	3.86
	Hybrid	2.47–4.60	3.86	3.93
	BCEP, EB	3.11–4.32	3.94	4.07, 4.14
	Hybrid, EB	3.79–4.02	3.94	–
	All	2.47–4.60	3.88	3.93
$\log(L/L_\odot)$	BCEP	3.45–5.34	4.19	4.18
	Hybrid	2.74–5.15	4.08	4.04
	BCEP, EB	3.81–4.94	4.35	–
	Hybrid, EB	3.82–4.98	4.09	–
	All	2.74–5.34	4.13	4.18
Q (d)	BCEP	0.015–0.084	0.035	0.036
	Hybrid	0.007–0.067	0.032	0.036
	BCEP, EB	0.025–0.038	0.027	–
	Hybrid, EB	0.021–0.094	0.023	–
	All	0.007–0.094	0.033	0.036
f_1 ($c\,d^{-1}$)	BCEP	3.28–16.63	5.84	5.08
	Hybrid	3.31–16.71	6.32	6.12
	BCEP, EB	3.78–13.41	5.80	–
	Hybrid, EB	4.34–9.18	6.77	–
	All	3.28–16.71	6.11	5.60
A_1 (PPT)	BCEP	0.14–135.58	11.51	5.62
	Hybrid	0.07–54.81	7.11	5.62
	BCEP, EB	0.91–38.50	7.50	–
	Hybrid, EB	5.78–36.84	12.05	–
	All	0.07–135.58	8.70	5.62

NOTE—Peak refers to the highest-bin center. When two bins share the highest count, all corresponding centers are listed. Peaks are not reported for samples with fewer than 40 data points.

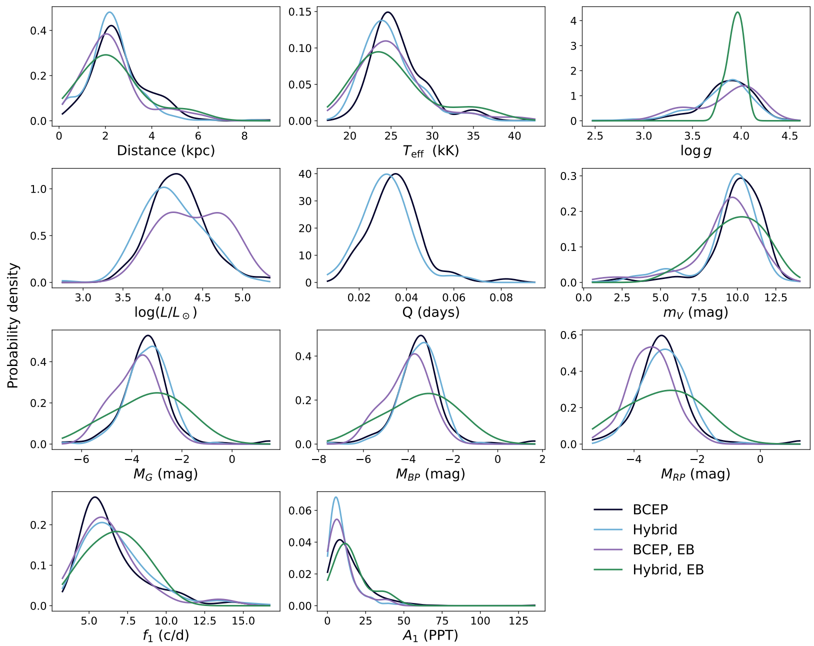

Figure G5. Kernel density estimates of the stellar and pulsation parameter distributions for the different variability classifications.

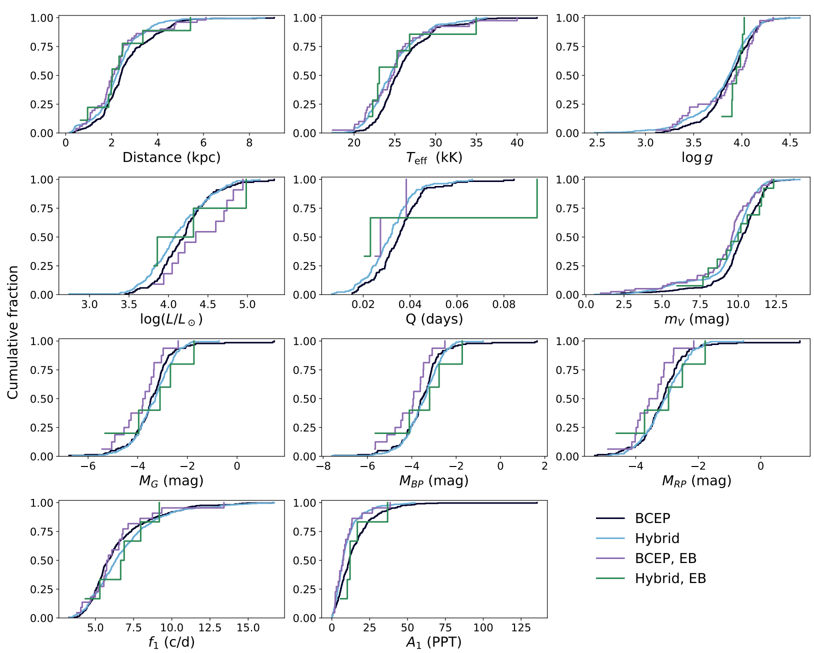

Figure G6. Empirical cumulative distribution functions of the stellar and pulsation parameters for the different variability classifications.

Table G7. Gaussian-mixture BIC comparisons and two-sample KS-test results for the BCEP and Hybrid distributions.

Parameter	Class	N	BIC(1)	BIC(2)	ΔBIC	$D_{\rm KS}$	$p_{\rm raw}$	$p_{\rm BH}$
Distance	BCEP	329	1072.68	1041.42	31.26	0.12	0.005889	0.011266
	Hybrid	454	1374.78	1336.47	38.31	0.12	0.005889	0.011266
$T_{\rm eff}$	BCEP	278	1486.17	1431.51	54.66	0.19	9.612×10^{-6}	3.574×10^{-5}
	Hybrid	380	2006.24	1961.24	45.00	0.19	9.612×10^{-6}	3.574×10^{-5}
$\log g$	BCEP	278	15.74	17.82	−2.08	0.08	0.188219	0.226449
	Hybrid	380	180.73	130.09	50.64	0.08	0.188219	0.226449
$\log(L/L_\odot)$	BCEP	120	94.34	102.19	−7.84	0.15	0.069025	0.108467
	Hybrid	159	153.28	167.98	−14.70	0.15	0.069025	0.108467
Q	BCEP	125	−756.46	−765.19	8.73	0.21	0.006145	0.011266
	Hybrid	135	−838.82	−831.82	−7.00	0.21	0.006145	0.011266
m_V	BCEP	354	1423.13	1269.16	153.97	0.17	9.748×10^{-6}	3.574×10^{-5}
	Hybrid	527	2247.85	1945.31	302.54	0.17	9.748×10^{-6}	3.574×10^{-5}
M_G	BCEP	143	416.51	381.98	34.52	0.12	0.200849	0.226449
	Hybrid	185	456.76	467.28	−10.53	0.12	0.200849	0.226449
M_{BP}	BCEP	143	438.70	400.24	38.46	0.12	0.205863	0.226449
	Hybrid	185	478.43	483.74	−5.31	0.12	0.205863	0.226449
M_{RP}	BCEP	143	371.62	340.28	31.35	0.11	0.229426	0.229426
	Hybrid	185	406.06	422.80	−16.73	0.11	0.229426	0.229426
f_1	BCEP	342	1509.10	1366.52	142.58	0.13	0.002541	0.006988
	Hybrid	421	1920.03	1824.35	95.68	0.13	0.002541	0.006988
A_1	BCEP	342	2766.13	2625.03	141.10	0.25	6.356×10^{-11}	6.991×10^{-10}
	Hybrid	421	3046.87	2814.42	232.45	0.25	6.356×10^{-11}	6.991×10^{-10}

Note—BIC(1) and BIC(2) are the Bayesian information criteria for the one- and two-component Gaussian-mixture models, respectively, and ΔBIC = BIC(1) − BIC(2); $D_{\rm KS}$ is the two-sample Kolmogorov–Smirnov statistic comparing the BCEP and Hybrid samples.

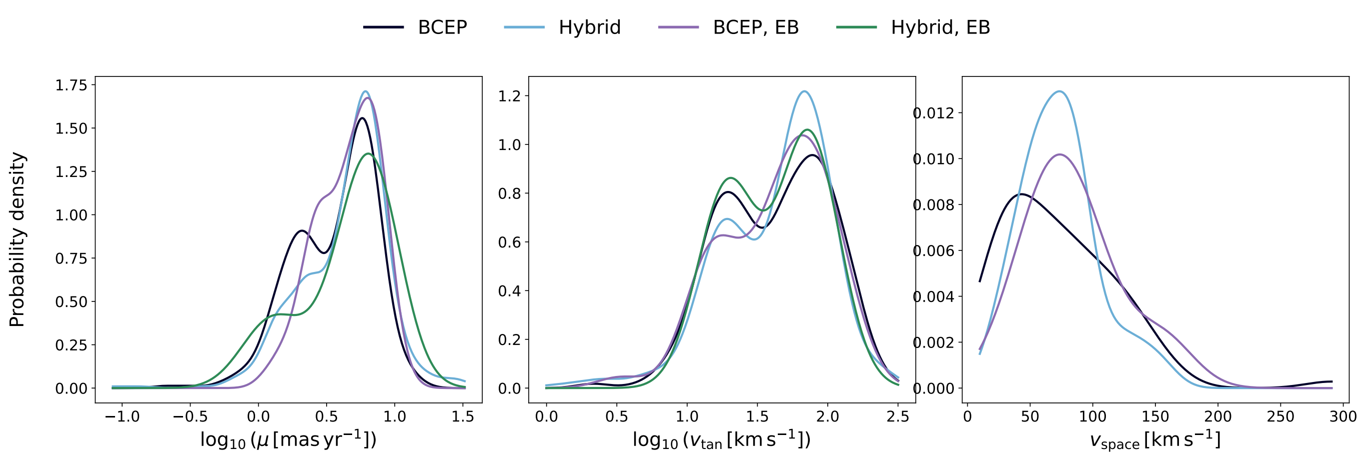

Figure H7. Kernel density estimates of the proper-motion (left), tangential-velocity (middle), and space-velocity (right) distributions for the different classifications.

Aerts, C., De Cat, P., De Ridder, J., et al. 2006, A&A, 449, 305, doi: 10.1051/0004-6361:20054142

Aerts, C., Thoul, A., Daszynska, J., et al. 2003, Science (New York, N.Y.), 300, 1926, doi: 10.1126/science.1084993

Antoci, V., Handler, G., Hareter, M., Kuschnig, R., & Matthews, J. M. 2009, in American Institute of Physics Conference Series, Vol. 1170, Stellar Pulsation: Challenges for Theory and Observation, ed. J. A. Guzik & P. A. Bradley (AIP), 373–375, doi: 10.1063/1.3246516

Astropy Collaboration, Robitaille, T. P., Tollerud, E. J., et al. 2013, A&A, 558, A33, doi: 10.1051/0004-6361/201322068

Table H8. Stars with exceptional tangential velocities or directions relative to the Galactic plane.

TIC	$v_{\rm tan}$ ($\rm km\,s^{-1}$)	$\theta_{\rm GP}$ (deg)
Exceptional tangential velocity only		
352229000	316.878	−42.632
130720430	272.716	+6.249
332791486	266.086	+4.430
4030832	252.942	−5.609
446463792	250.211	+2.802
439747589	238.266	−9.687
41548989	228.003	+5.226
384540878	225.792	−14.069
80333031	219.183	−12.980
466208395	212.342	−0.343
401975322	208.417	−36.620
49217799	202.705	−35.270
213272222	193.390	−3.627
303416677	192.022	−0.524
Exceptional direction with $v_{\rm tan} > 20$ $\rm km\,s^{-1}$		
468498193	85.444	−81.922
301263808	40.395	−78.744
173767386	38.103	−76.301
71737416	26.432	−75.601
60433558	32.519	−74.453
433182985	28.830	−73.656
65564230	59.189	−71.955
34003157	81.070	−71.056
407463080	27.165	+70.214
374982274	20.477	−69.734
198165966	56.492	+68.172
15644631	26.194	−67.711
374478187	28.005	−64.951
121679880	22.886	−64.901
247649462	21.041	−63.292
422666117	127.441	+61.320
113404375	20.242	−60.407
380870688	22.871	−58.318
196639455	22.352	−57.203
308954763	31.723	−56.910
349351160	88.306	−55.204
28565824	28.571	+55.112
347378183	22.773	−54.252
314393072	24.025	−53.587
246097860	118.657	−53.456
390432717	75.082	−53.035
195407015	26.632	−52.789
452188490	59.663	−52.303
435123631	46.919	+51.610
211408145	166.723	−51.074
34803944	86.095	+50.109
65516748	85.088	−49.977
359424879	61.295	−49.152
76426958	82.172	−48.762
435742094	54.003	+48.258
217755761	33.306	−47.553
458246279	25.792	−47.099
Both criteria		
98084512	244.952	+88.314
57384424	229.423	−67.131

Note— The angle $\theta_{\rm GP}$ gives the signed direction of the tangential velocity relative to the Galactic plane. Positive and negative values indicate motion toward positive and negative Galactic latitude, respectively.

Astropy Collaboration, Price-Whelan, A. M., Sipőcz, B. M., et al. 2018, AJ, 156, 123, doi: 10.3847/1538-3881/aabc4f

Astropy Collaboration, Price-Whelan, A. M., Lim, P. L., et al. 2022, ApJ, 935, 167, doi: 10.3847/1538-4357/ac7c74

Bailer-Jones, C. A. L. 2015, PASP, 127, 994, doi: 10.1086/683116

Bakış, V., Hensberge, H., Bilir, S., et al. 2014, AJ, 147, 149, doi: 10.1088/0004-6256/147/6/149

Bakos, G., Noyes, R. W., Kovács, G., et al. 2004a, PASP, 116, 266, doi: 10.1086/382735

—. 2004b, PASP, 116, 266, doi: 10.1086/382735

Balona, L. A., Baran, A. S., Daszyńska-Daszkiewicz, J., & De Cat, P. 2015, MNRAS, 451, 1445, doi: 10.1093/mnras/stv1017

Balona, L. A., & Ozuyar, D. 2020, MNRAS, 493, 2528, doi: 10.1093/mnras/staa389

Balona, L. A., Pigulski, A., De Cat, P., et al. 2011, MNRAS, 413, 2403, doi: 10.1111/j.1365-2966.2011.18311.x

Baran, A. S., & Koen, C. 2021, AcA, 71, 113, doi: 10.32023/0001-5237/71.2.3

Bass, G., & Borne, K. 2016, MNRAS, 459, 3721, doi: 10.1093/mnras/stw810

Bellm, E. C., Kulkarni, S. R., Graham, M. J., et al. 2019, PASP, 131, 018002, doi: 10.1088/1538-3873/aaecbe

Benjamini, Y., & Hochberg, Y. 1995, Journal of the Royal Statistical Society: Series B (Methodological), 57, 289, doi: 10.1111/j.2517-6161.1995.tb02031.x

Bognár, Z., Kalup, C., Sódor, Á., Charpinet, S., & Hermes, J. J. 2018, MNRAS, 478, 2676, doi: 10.1093/mnras/sty1393

Borucki, W. J., Koch, D., Basri, G., et al. 2010, Science, 327, 977, doi: 10.1126/science.1185402

Bouzid, M. Y., & Sterken, C. 2004, in Astronomical Society of the Pacific Conference Series, Vol. 318, Spectroscopically and Spatially Resolving the Components of the Close Binary Stars, ed. R. W. Hilditch, H. Hensberge, & K. Pavlovski, 288–290

Bowman, D. M. 2020, Frontiers in Astronomy and Space Sciences, 7, doi: 10.3389/fspas.2020.578584

Bowman, D. M., Vandenbussche, B., Sana, H., et al. 2022, A&A, 658, A96, doi: 10.1051/0004-6361/202142375

Bramall, D. G., Sharples, R., Tyas, L., et al. 2010, in Society of Photo-Optical Instrumentation Engineers (SPIE) Conference Series, Vol. 7735, Ground-based and Airborne Instrumentation for Astronomy III, ed. I. S. McLean, S. K. Ramsay, & H. Takami, 77354F, doi: 10.1117/12.856382

Bramall, D. G., Schmoll, J., Tyas, L. M. G., et al. 2012, in Society of Photo-Optical Instrumentation Engineers (SPIE) Conference Series, Vol. 8446, Ground-based and Airborne Instrumentation for Astronomy IV, ed. I. S. McLean, S. K. Ramsay, & H. Takami, 84460A, doi: 10.1117/12.925935

Brott, I., de Mink, S. E., Cantiello, M., et al. 2011, A&A, 530, A115, doi: 10.1051/0004-6361/201016113

Brown, T. M., Baliber, N., Bianco, F. B., et al. 2013, PASP, 125, 1031, doi: 10.1086/673168

Buckley, D. A. H., Swart, G. P., & Meiring, J. G. 2006, in Society of Photo-Optical Instrumentation Engineers (SPIE) Conference Series, Vol. 6267, Ground-based and Airborne Telescopes, ed. L. M. Stepp, 62670Z, doi: 10.1117/12.673750

Burssens, S., Bowman, D. M., Aerts, C., et al. 2019, MNRAS, 489, 1304, doi: 10.1093/mnras/stz2165

Burssens, S., Simón-Díaz, S., Bowman, D. M., et al. 2020, A&A, 639, A81, doi: 10.1051/0004-6361/202037700

Burssens, S., Bowman, D. M., Michielsen, M., et al. 2023, Nature Astronomy, 7, 913, doi: 10.1038/s41550-023-01978-y

Catanzaro, G., Leone, F., & Dall, T. H. 2004, A&A, 425, 641, doi: 10.1051/0004-6361:20040558

Çakırlı, Ö., Hoyman, B., Özdarcan, O., & Bilir, S. 2025, MNRAS, 543, 2958, doi: 10.1093/mnras/staf1623

Chakraborty, A., Jose, J., & Carciofi, A. C. 2025, MNRAS, 541, 1866, doi: 10.1093/mnras/staf1104

Chen, X., Ding, X., Cheng, L., et al. 2022, ApJS, 263, 34, doi: 10.3847/1538-4365/aca284

Cox, A. N., ed. 2000, Allen's Astrophysical Quantities, 4th edn. (New York: Springer)

Crause, L. A., Sharples, R. M., Bramall, D. G., et al. 2014, in Society of Photo-Optical Instrumentation Engineers (SPIE) Conference Series, Vol. 9147, Ground-based and Airborne Instrumentation for Astronomy V, ed. S. K. Ramsay, I. S. McLean, & H. Takami, 91476T, doi: 10.1117/12.2055635

Crawford, S. M., Still, M., Schellart, P., et al. 2010, in Society of Photo-Optical Instrumentation Engineers (SPIE) Conference Series, Vol. 7737, Observatory Operations: Strategies, Processes, and Systems III, ed. D. R. Silva, A. B. Peck, & B. T. Soifer, 773725, doi: 10.1117/12.857000

Creevey, O. L., Sordo, R., Pailler, F., et al. 2023, A&A, 674, A26, doi: 10.1051/0004-6361/202243688

De Cat, P., Briquet, M., Aerts, C., et al. 2006, Communications in Asteroseismology, 147, 48, doi: 10.1553/cia147s48

De Ridder, J., Telting, J. H., Balona, L. A., et al. 2004, MNRAS, 351, 324, doi: 10.1111/j.1365-2966.2004.07791.x

Degroote, P., Aerts, C., Ollivier, M., et al. 2009, A&A, 506, 471, doi: 10.1051/0004-6361/200911884

Díaz-Fraile, D., Rodríguez, E., & Amado, P. J. 2014, A&A, 568, A32, doi: 10.1051/0004-6361/201423478

Drobek, D., Pigulski, A., Shobbrook, R. R., & Narwid, A. 2013, AcA, 63, 339, doi: 10.48550/arXiv.1309.7371

Dziembowski, W. A., & Pamiatnykh, A. A. 1993, MNRAS, 262, 204, doi: 10.1093/mnras/262.1.204

Eze, C. I., & Handler, G. 2024, ApJS, 272, 25, doi: 10.3847/1538-4365/ad39c5

Fitzgerald, M. P., & Miller, M. L. 1983, PASP, 95, 361, doi: 10.1086/131174

Fitzpatrick, E. L. 2004, in Astronomical Society of the Pacific Conference Series, Vol. 309, Astrophysics of Dust, ed. A. N. Witt, G. C. Clayton, & B. T. Draine, 33, doi: 10.48550/arXiv.astro-ph/0401344

Fouesneau, M., Frémat, Y., Andrae, R., et al. 2023, A&A, 674, A28, doi: 10.1051/0004-6361/202243919

Freedman, D., & Diaconis, P. 1981, Zeitschrift für Wahrscheinlichkeitstheorie und Verwandte Gebiete, 57, 453, doi: 10.1007/BF01025868

Fritzewski, D. J., Vanrespaille, M., Aerts, C., et al. 2025a, A&A, 698, A253, doi: 10.1051/0004-6361/202451721

—. 2025b, A&A, 698, A253, doi: 10.1051/0004-6361/202451721

Gaia Collaboration, Prusti, T., de Bruijne, J. H. J., et al. 2016, A&A, 595, A1, doi: 10.1051/0004-6361/201629272

Gaia Collaboration, Brown, A. G. A., Vallenari, A., et al. 2021, A&A, 649, A1, doi: 10.1051/0004-6361/202039657

Gaia Collaboration, Vallenari, A., Brown, A. G. A., et al. 2023a, A&A, 674, A1, doi: 10.1051/0004-6361/202243940

Gaia Collaboration, De Ridder, J., Ripepi, V., et al. 2023b, A&A, 674, A36, doi: 10.1051/0004-6361/202243767

Garrison, R. F., Hiltner, W. A., & Schild, R. E. 1977, ApJS, 35, 111, doi: 10.1086/190468

Gray, D. F. 2005, The Observation and Analysis of Stellar Photospheres, doi: 10.1017/CBO9781316036570

Green, G. 2018, The Journal of Open Source Software, 3, 695, doi: 10.21105/joss.00695

Green, G. M., Schlafly, E., Zucker, C., Speagle, J. S., & Finkbeiner, D. 2019, ApJ, 887, 93, doi: 10.3847/1538-4357/ab5362

Handler, G. 2005, Information Bulletin on Variable Stars, 5667, 1

Handler, G., & Meingast, S. 2011, A&A, 533, A70, doi: 10.1051/0004-6361/201116874

Handler, G., Shobbrook, R. R., & Mokgwetsi, T. 2005, MNRAS, 362, 612, doi: 10.1111/j.1365-2966.2005.09341.x

Handler, G., Jerzykiewicz, M., Rodríguez, E., et al. 2006a, MNRAS, 365, 327, doi: 10.1111/j.1365-2966.2005.09728.x

—. 2006b, MNRAS, 365, 327, doi: 10.1111/j.1365-2966.2005.09728.x

Handler, G., Matthews, J. M., Eaton, J. A., et al. 2009, ApJL, 698, L56, doi: 10.1088/0004-637X/698/1/L56

Handler, G., Shobbrook, R. R., Uytterhoeven, K., et al. 2012a, MNRAS, 424, 2380, doi: 10.1111/j.1365-2966.2012.21414.x

—. 2012b, MNRAS, 424, 2380, doi: 10.1111/j.1365-2966.2012.21414.x

Herbst, W. 1975, AJ, 80, 212, doi: 10.1086/111734

Hey, D., & Aerts, C. 2024, A&A, 688, A93, doi: 10.1051/0004-6361/202450489

Hill, G. 1967, ApJS, 14, 301, doi: 10.1086/190157

Holgado, G., Simón-Díaz, S., & Herrero, A. 2025, A&A, 703, A175, doi: 10.1051/0004-6361/202556713

Houk, N. 1978, Michigan catalogue of two-dimensional spectral types for the HD stars

—. 1982, Michigan Catalogue of Two-dimensional Spectral Types for the HD stars. Volume_3. Declinations -40_f0 to -26_f0.

Houk, N., & Cowley, A. P. 1975, University of Michigan Catalogue of two-dimensional spectral types for the HD stars. Volume I. Declinations -90_ to -53_f0.

Houk, N., & Smith-Moore, M. 1988, Michigan Catalogue of Two-dimensional Spectral Types for the HD Stars. Volume 4, Declinations -26°.0 to -12°.0., Vol. 4

Houk, N., & Swift, C. 1999, Michigan Spectral Survey, 5, 0

Hu, J.-H., Chen, H.-C., Chen, Y.-T., et al. 2011, PASP, 123, 671, doi: 10.1086/660819

Huang, C. X., Vanderburg, A., Pál, A., et al. 2020, Research Notes of the American Astronomical Society, 4, 204, doi: 10.3847/2515-5172/abca2e

Hubeny, I., & Lanz, T. 1995, ApJ, 439, 875, doi: 10.1086/175226

Hubrig, S., Briquet, M., De Cat, P., et al. 2009, Astronomische Nachrichten, 330, 317, doi: 10.1002/asna.200811187

IJspeert, L. W., Tkachenko, A., Johnston, C., et al. 2024, A&A, 685, A62, doi: 10.1051/0004-6361/202349079

Jaschek, C., & Gomez, A. E. 1998, A&A, 330, 619

Jenkins, J. M., Twicken, J. D., McCauliff, S., et al. 2016, in Society of Photo-Optical Instrumentation Engineers (SPIE) Conference Series, Vol. 9913, Software and Cyberinfrastructure for Astronomy IV, ed. G. Chiozzi & J. C. Guzman, 99133E, doi: 10.1117/12.2233418

Jurcsik, J., Sodor, A., & Hajdu, G. 2009, Information Bulletin on Variable Stars, 5881, 1

Kemp, A., Vrancken, J., Mombarg, J. S. G., et al. 2025, A&A, 704, A280, doi: 10.1051/0004-6361/202557362

Kochanek, C. S., Shappee, B. J., Stanek, K. Z., et al. 2017, PASP, 129, 104502, doi: 10.1088/1538-3873/aa80d9

Kołaczek-Szymański, P. A., Pigulski, A., Michalska, G., Moździerski, D., & Różański, T. 2021, A&A, 647, A12, doi: 10.1051/0004-6361/202039553

Kurtz, D. W., Shibahashi, H., Murphy, S. J., Bedding, T. R., & Bowman, D. M. 2015, MNRAS, 450, 3015, doi: 10.1093/mnras/stv868

Labadie-Bartz, J., Handler, G., Pepper, J., et al. 2020, AJ, 160, 32, doi: 10.3847/1538-3881/ab952c

Lata, S., Pandey, A. K., Kesh Yadav, R., et al. 2019, AJ, 158, 68, doi: 10.3847/1538-3881/ab298c

Lata, S., Pandey, A. K., Panwar, N., et al. 2016, MNRAS, 456, 2505, doi: 10.1093/mnras/stv2800

Lata, S., Yadav, R. K., Pandey, A. K., et al. 2014, MNRAS, 442, 273, doi: 10.1093/mnras/stu726

Laur, J., Kolka, I., Eenmäe, T., Tuvikene, T., & Leedjärv, L. 2017, A&A, 598, A108, doi: 10.1051/0004-6361/201629395

Lee, J. W., & Hong, K. 2021, AJ, 161, 32, doi: 10.3847/1538-3881/abbfff

Lehmann, H., Tkachenko, A., Semaan, T., et al. 2011, A&A, 526, A124, doi: 10.1051/0004-6361/201015769

Lightkurve Collaboration, Cardoso, J. V. d. M., Hedges, C., et al. 2018, Lightkurve: Kepler and TESS time series analysis in Python, Astrophysics Source Code Library, record ascl:1812.013

Lindegren, L., Bastian, U., Biermann, M., et al. 2021, A&A, 649, A4, doi: 10.1051/0004-6361/202039653

Luri, X., Brown, A. G. A., Sarro, L. M., et al. 2018, A&A, 616, A9, doi: 10.1051/0004-6361/201832964

Majewska-Świerzbinowicz, A., Pigulski, A., Szabó, R., & Csubry, Z. 2008, in Journal of Physics Conference Series, Vol. 118, Journal of Physics Conference Series (IOP), 012068, doi: 10.1088/1742-6596/118/1/012068

Markova, N., & Puls, J. 2008, A&A, 478, 823, doi: 10.1051/0004-6361:20077919

McNamara, B. J., Jackiewicz, J., & McKeever, J. 2012, AJ, 143, 101, doi: 10.1088/0004-6256/143/4/101

Meingast, S., Handler, G., & Shobbrook, R. R. 2013, A&A, 559, A108, doi: 10.1051/0004-6361/201220823

Michalska, G., Pigulski, A., Stelicki, M., & Narwid, A. 2009, AcA, 59, 349, doi: 10.48550/arXiv.0910.3672

Moskalik, P., & Dziembowski, W. A. 1992, A&A, 256, L5

Moździerski, D., Pigulski, A., Kołaczkowski, Z., et al. 2019, A&A, 632, A95, doi: 10.1051/0004-6361/201936418

Münch, L. 1952, Boletin de los Observatorios Tonantzintla y Tacubaya, 1, 1

Murphy, S. J. 2012, MNRAS, 422, 665, doi: 10.1111/j.1365-2966.2012.20644.x

Narwid, A., Kołaczkowski, Z., Pigulski, A., & Ramza, T. 2006, Mem. Soc. Astron. Italiana, 77, 342, doi: 10.48550/arXiv.astro-ph/0510073

Nazé, Y., Rauw, G., Kołaczek-Szymański, P. A., Britavskiy, N., & Labadie-Bartz, J. 2025, A&A, 703, A239, doi: 10.1051/0004-6361/202556441

Neiner, C., & Floquet, M. 2011, in SF2A-2011: Proceedings of the Annual meeting of the French Society of Astronomy and Astrophysics, ed. G. Alecian, K. Belkacem, R. Samadi, & D. Valls-Gabaud, 231–233

Nieva, M.-F., & Przybilla, N. 2012, A&A, 539, A143, doi: 10.1051/0004-6361/201118158

O'Donoghue, D., Kilkenny, D., Koen, C., et al. 2013, MNRAS, 431, 240, doi: 10.1093/mnras/stt158

Paparó, M., Chadid, M., Chapellier, E., et al. 2011, A&A, 531, A135, doi: 10.1051/0004-6361/201116579

Pápics, P. I., Tkachenko, A., Aerts, C., et al. 2013, A&A, 553, A127, doi: 10.1051/0004-6361/201321088

Pedersen, M. G., Escorza, A., Pápics, P. I., & Aerts, C. 2020, MNRAS, 495, 2738, doi: 10.1093/mnras/staa1292

Pedregosa, F., Varoquaux, G., Gramfort, A., et al. 2011, Journal of Machine Learning Research, 12, 2825

Pepper, J., Kuhn, R. B., Siverd, R., James, D., & Stassun, K. 2012, PASP, 124, 230, doi: 10.1086/665044

Pepper, J., Pogge, R. W., DePoy, D. L., et al. 2007, PASP, 119, 923, doi: 10.1086/521836

Pietrukowicz, P., Olech, A., Wisniewski, M., et al. 2006, AcA, 56, 267, doi: 10.48550/arXiv.astro-ph/0609155

Pietrukowicz, P., Dziembowski, W. A., Mróz, P., et al. 2013, AcA, 63, 379, doi: 10.48550/arXiv.1311.5894

Pigulski, A., Jerzykiewicz, M., & Kopacki, G. 1997, AcA, 47, 365

Pigulski, A., & Michalska, G. 2007, AcA, 57, 61, doi: 10.48550/arXiv.astro-ph/0703614

Pigulski, A., & Pojmański, G. 2007, in IAU Symposium, Vol. 240, Binary Stars as Critical Tools & Tests in Contemporary Astrophysics, ed. W. I. Hartkopf, P. Harmanec, & E. F. Guinan, 456–458, doi: 10.1017/S1743921307004449

Pigulski, A., & Pojmański, G. 2008a, A&A, 477, 917, doi: 10.1051/0004-6361:20078581

—. 2008b, A&A, 477, 907, doi: 10.1051/0004-6361:20078580

Pojmanski, G. 1997a, AcA, 47, 467. https://arxiv.org/abs/astro-ph/9712146

—. 1997b, AcA, 47, 467. https://arxiv.org/abs/astro-ph/9712146

Pojmański, G. 2001a, in Astronomical Society of the Pacific Conference Series, Vol. 246, IAU Colloq. 183: Small Telescope Astronomy on Global Scales, ed. B. Paczynski, W.-P. Chen, & C. Lemme, 53

Pojmański, G. 2001b, in Astronomical Society of the Pacific Conference Series, Vol. 246, IAU Colloq. 183: Small Telescope Astronomy on Global Scales, ed. B. Paczynski, W.-P. Chen, & C. Lemme, 53

Reed, B. C. 2003, AJ, 125, 2531, doi: 10.1086/374771

Ricker, G. R., Winn, J. N., Vanderspek, R., et al. 2015, Journal of Astronomical Telescopes, Instruments, and Systems, 1, 014003, doi: 10.1117/1.JATIS.1.1.014003

Rimoldini, L., Holl, B., Gavras, P., et al. 2023, A&A, 674, A14, doi: 10.1051/0004-6361/202245591

Saesen, S., Briquet, M., Aerts, C., Miglio, A., & Carrier, F. 2014, in IAU Symposium, Vol. 301, Precision Asteroseismology, ed. J. A. Guzik, W. J. Chaplin, G. Handler, & A. Pigulski, 479–480, doi: 10.1017/S1743921313015147

Samus', N. N., Kazarovets, E. V., Durlevich, O. V., Kireeva, N. N., & Pastukhova, E. N. 2017, Astronomy Reports, 61, 80, doi: 10.1134/S1063772917010085

Samus', N. N., Goranskii, V. P., Durlevich, O. V., et al. 2003, Astronomy Letters, 29, 468, doi: 10.1134/1.1589864

Sarro, L. M., Debosscher, J., Neiner, C., et al. 2013, A&A, 550, A120, doi: 10.1051/0004-6361/201220184

Schild, R. E. 1970, ApJ, 161, 855, doi: 10.1086/150589

Shi, X.-d., Qian, S.-b., Zhu, L.-y., et al. 2024, ApJS, 271, 28, doi: 10.3847/1538-4365/ad1f66

—. 2025, ApJS, 281, 17, doi: 10.3847/1538-4365/ae101e

—. 2023, ApJS, 265, 33, doi: 10.3847/1538-4365/acba91

Shitrit, N., & Arcavi, I. 2024, AJ, 167, 65, doi: 10.3847/1538-3881/ad1514

Skarka, M., Mašek, M., Brát, L., et al. 2017, Open European Journal on Variable Stars, 185, 1, doi: 10.48550/arXiv.1709.08851

Sota, A., Maíz Apellániz, J., Walborn, N. R., et al. 2011, ApJS, 193, 24, doi: 10.1088/0067-0049/193/2/24

Southworth, J., & Bowman, D. M. 2022, MNRAS, 513, 3191, doi: 10.1093/mnras/stac875

Southworth, J., Bowman, D. M., Tkachenko, A., & Pavlovski, K. 2020, MNRAS, 497, L19, doi: 10.1093/mnrasl/slaa091

Stankov, A., & Handler, G. 2005, ApJS, 158, 193, doi: 10.1086/429408

Stassun, K. G., Torres, G., Johnston, C., et al. 2021, ApJ, 910, 133, doi: 10.3847/1538-4357/abe5a8

Telting, J., Schrijvers, C., Ilyin, I., et al. 2007, in Astronomical Society of the Pacific Conference Series, Vol. 361, Active OB-Stars: Laboratories for Stellare and Circumstellar Physics, ed. A. T. Okazaki, S. P. Owocki, & S. Stefl, 64

Thomson-Paressant, K., Bowman, D. M., Nardini, F., et al. 2026, MNRAS, 551, stag1493, doi: 10.1093/mnras/stag1493

Townsend, R. H. D. 2000, MNRAS, 318, 1, doi: 10.1046/j.1365-8711.2000.03536.x

Udalski, A., Szymanski, M., Kaluzny, J., Kubiak, M., & Mateo, M. 1992, AcA, 42, 253

Udalski, A., Szymański, M. K., & Szymański, G. 2015, AcA, 65, 1. https://arxiv.org/abs/1504.05966

Ulusoy, C., Niemczura, E., Ulaş, B., & Gülmez, T. 2013, NewA, 23, 55, doi: 10.1016/j.newast.2013.02.005

Ushomirsky, G., & Bildsten, L. 1998, ApJL, 497, L101, doi: 10.1086/311282

Uytterhoeven, K., Moya, A., Grigahcène, A., et al. 2011, A&A, 534, A125, doi: 10.1051/0004-6361/201117368

Vanrespaille, M., Fritzewski, D. J., Vanlaer, V., & Aerts, C. 2026, arXiv e-prints, arXiv:2607.10834, doi: 10.48550/arXiv.2607.10834

Virtanen, P., Gommers, R., Oliphant, T. E., et al. 2020, Nature Methods, 17, 261, doi: 10.1038/s41592-019-0686-2

Walker, G. A. H. 2008, in Journal of Physics Conference Series, Vol. 118, Journal of Physics Conference Series (IOP), 012013, doi: 10.1088/1742-6596/118/1/012013

Watson, C., Henden, A. A., & Price, A. 2022, VizieR Online Data Catalog: AAVSO International Variable Star Index VSX (Watson+, 2006-), VizieR On-line Data Catalog: B/vsx. Originally published in: 2006SASS...25...47W

Wenger, M., Ochsenbein, F., Egret, D., et al. 2000, A&AS, 143, 9, doi: 10.1051/aas:2000332

Xue, H.-F., Fu, J.-N., Mowlavi, N., et al. 2019, MNRAS, 482, 658, doi: 10.1093/mnras/sty2627

Zhang, X. B., Luo, C. Q., & Fu, J. N. 2012, AJ, 144, 86, doi: 10.1088/0004-6256/144/3/86

Zhuo, J., Deng, L.-C., Wang, K., et al. 2021, Research in Astronomy and Astrophysics, 21, 227, doi: 10.1088/1674-4527/21/9/227

Zummer, M., Harmanec, P., Barlow, B., Blackford, M., & Švrčková, J. 2026, A&A, 705, A60, doi: 10.1051/0004-6361/202557637